

Contrasting subduction–exhumation paths in the blueschists of the Anarak Metamorphic Complex (Central Iran)

S. ZANCHETTA*†, N. MALASPINA*, A. ZANCHI*, L. BENCIOLINI‡, S. MARTIN§, H.R. JAVADI¶ & M. KOUHPEYMA¶

*Dipartimento di Scienze dell’Ambiente e della Terra, Piazza della Scienza 4, 20126 Milano, Italy

‡Dipartimento di Fisica, Chimica e Ambiente, Università degli Studi di Udine, Italy

§Dipartimento di Geoscienze, Università degli Studi di Padova, Italy

¶Geological Survey of Iran, Azadi Square, Meraj Avenue, 13185-1494 Tehran, Iran

(Received 2 November 2016; accepted 17 February 2017; first published online 3 April 2017)

Abstract – The Anarak Metamorphic Complex, localized in Central Iran, is a fossil accretionary wedge composed of several tectonometamorphic units. Some of these, the Chah Gorbek, the Morghab and the Ophiolitic complexes, contain mafic rocks that have been metamorphosed at high-pressure–low-temperature conditions. Such units have been stacked together and later refolded during the final stages of exhumation. Structural analysis at the mesoscale recognized at least three deformation events. Microstructural analyses, mineral chemistry and thermodynamic modelling reveal that the mafic schists followed contrasting P – T paths during their tectonometamorphic evolutions. In the schists of the Chah Gorbek and Ophiolitic complexes an early greenschist-facies stage was later overprinted by blueschist-facies phase assemblages with suggested peak conditions of 390–440 °C at 0.6–0.9 GPa for the meta-basalt within the Ophiolitic Complex and 320–380 °C at 0.6–0.9 GPa for the blueschists of the Chah Gorbek Complex. P – T conditions at metamorphic peak were 410–450 °C at 0.78–0.9 GPa for the Morghab blueschists, but they are reached before a greenschist-facies re-equilibration. Compositional zoning of amphiboles and epidotes of this greenschist-facies stage suggests a renewed pressure increase at the end of this metamorphic stage. Based on these data we reconstructed a clockwise P – T path for the Morghab mafic schists and a counter-clockwise path for the Chah Gorbek blueschists and ophiolitic meta-basalts. Such contrasting metamorphic evolutions of tectonic units that were later accreted to the same wedge are indicative of the complex tectonic dynamics that occur within accretionary–subduction complexes.

Keywords: Central Iran, mafic blueschists, accretionary wedge, P – T evolution

1. Introduction

The occurrence of mafic blueschists is considered one of the main points of evidence for oceanic subduction accompanied by the formation of an accretionary prism between the upper and the subducting plate (e.g. Ernst, 1973). Blueschist-facies rocks are mainly found to occur as large coherent terranes or as isolated blocks within a serpentinitic or pelitic matrix in tectonic mélangé complexes (Hsu, 1968).

The P – T conditions at metamorphic peak and the subduction–exhumation paths followed by blueschist-facies rocks strongly depend on the thermal regime during subduction, which in turn depends on the age and structure of the subducting plate (e.g. Cloos & Shreve, 1988*a,b*), and on the time at which the rocks are subducted with respect to subduction initiation (i.e. initial versus late-subducted blueschists). Depressed thermal regimes usually develop only after a few million years following subduction initiation (Gerya & Stockhert, 2006), and rock units that are subducted later may escape a first heating stage that is commonly experienced by units that are underplated in the nas-

cent accretionary wedge at subduction initiation (Ukar, 2012).

The common occurrence within a single accretionary complex of blueschists that have reached different depths and followed different subduction–exhumation paths (e.g. Agard *et al.* 2010) testifies to the complexity of the tectonic and thermal structure of an evolving accretionary wedge.

In Central Iran, the Anarak Metamorphic Complex (AMC) is interpreted as a fossil accretionary prism (Sharkovski, Susov & Krivyakin, 1984; Bagheri & Stampfli, 2008) developed in the framework of the northward subduction of the Palaeo-Tethys beneath the southern Eurasian margin (e.g. Şengör, 1979). The AMC consists of several units, some of which were metamorphosed at blueschist-facies conditions (Zanchi *et al.* 2009, 2015). The difference in lithological composition, metamorphic peak conditions and age of metamorphism led some authors to consider the AMC as a composite complex, formed during tectonic events that were separated in time and space.

In this paper, we address the petrographic and textural features of mafic blueschists of the AMC, in order to reveal the recrystallization stages and the deformation–metamorphism relationships in the Chah

†Author for correspondence: stefano.zanchetta@unimib.it

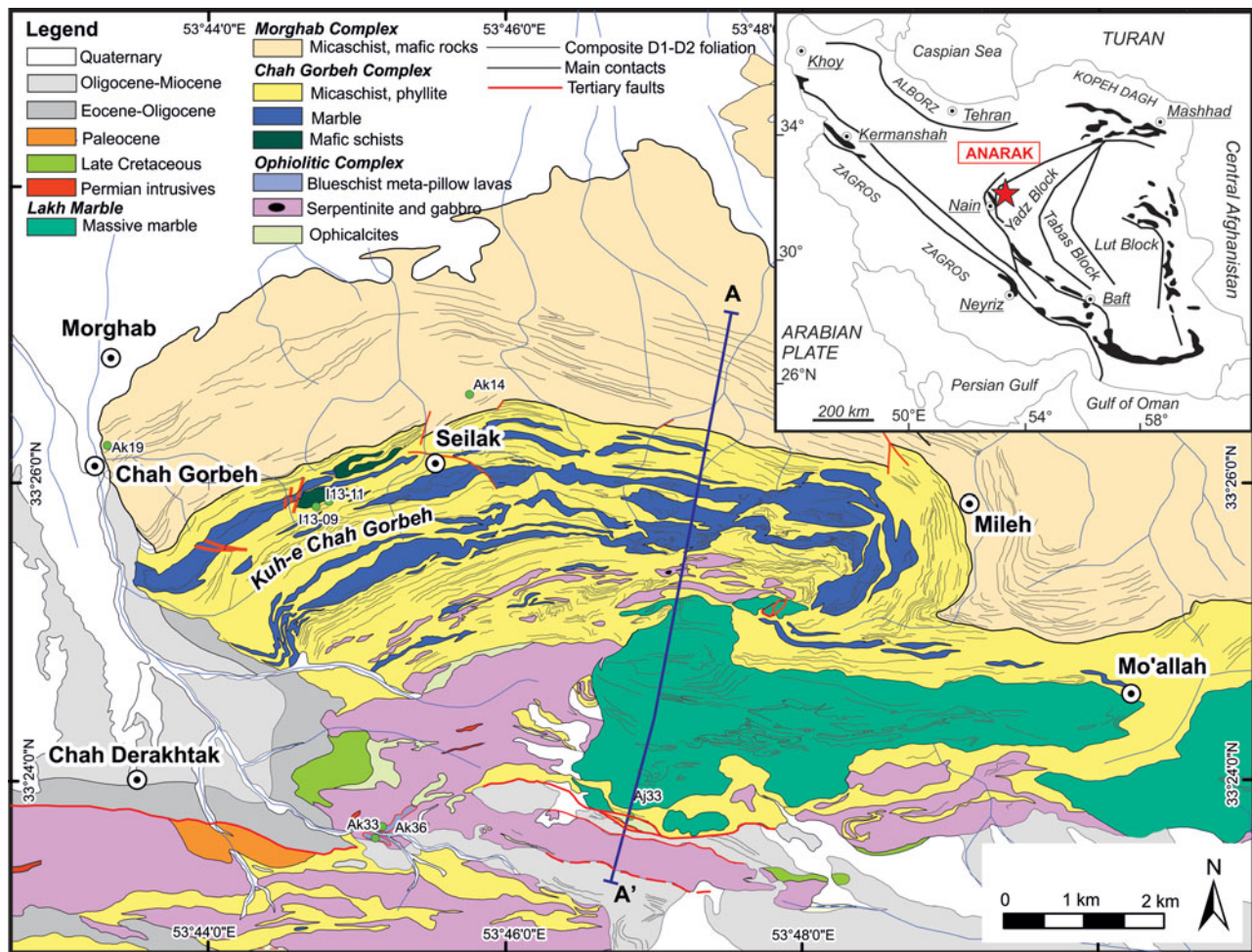


Figure 1. (Colour online) Geological map of the Anarak Metamorphic Complex with location of analysed samples. The trace of the geological cross-section in Figure 2 is here indicated. Modified after Zanchi *et al.* (2015).

Gorbah, Morghab and Ophiolitic complexes. We also performed thermodynamic modelling in order to estimate the P and T conditions of each metamorphic stage recognized in the analysed samples.

The whole dataset of petrographic, microstructural and thermodynamic data is then used to define the P – T trajectories of mafic blueschists from the three units. The results are then discussed in the context of accretionary wedge dynamics and AMC tectonic significance.

2. Geological setting

The AMC crops out in Central Iran, to the east of Nain (Fig. 1). It consists of several subunits exposed for *c.* 150 km in an E–W-trending belt, stacked together during polyphase metamorphic and deformation events (Sharkovski, Susov & Krivyakin, 1984; Bagheri & Stampfli, 2008; Zanchi *et al.* 2009; Buchs *et al.* 2013; Zanchi *et al.* 2015). The AMC is in tectonic contact with other metamorphic complexes and sedimentary successions of various ages and palaeogeographic affinities (Fig. 1). To the west, the Great Kavir – Doruneh fault system represents the contact

between the AMC and the Cretaceous ophiolites that border the entire Central–East Iranian Microcontinent (Ghasemi & Talbot, 2006). The southern limit of the AMC coincides with the NW border of the Yadz block whereas to the east the Jandaq complex, a magmatic–metamorphic unit with a poorly defined age (likely Carboniferous or pre-Carboniferous, Bagheri & Stampfli, 2008; Berra *et al.* 2017), is exposed. Finally, to the north of the AMC, the non-metamorphic Nakhllak ophiolite–sedimentary complex occurs (Balini *et al.* 2009). The contact between the AMC and the Nakhllak complex is not exposed, so the relationships existing between the complexes are not clear (Balini *et al.* 2009; Zanchi *et al.* 2009).

The AMC is composed of several subunits which display heterogeneous structural and metamorphic evolutions (Sharkovski, Susov & Krivyakin, 1984; Bagheri & Stampfli, 2008; Zanchi *et al.* 2009, 2015). The Morghab Complex largely consists of metapelitic schists with abundant interleaved quartzite and metabasite layers (Zanchi *et al.* 2015). Minor meta-volcanic rocks and amphibole-bearing gneisses occur in the Kuh-e Pol-e Khavand area (Fig. 1).

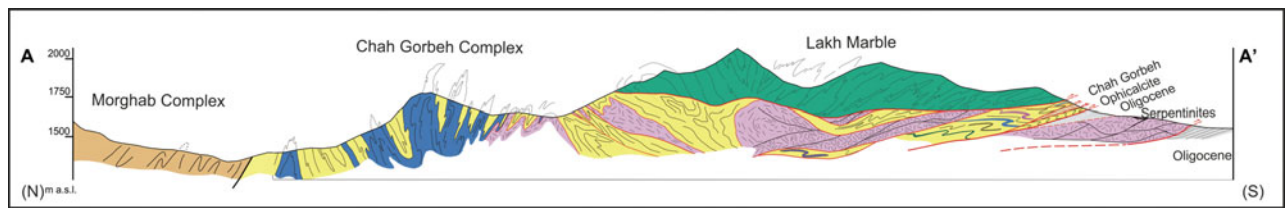


Figure 2. (Colour online) Schematic cross-section showing the main structural features of the AMC and the tectonic relationships between the CGC, MC and OC complexes and the overlying Lakh Marble. Modified after Zanchi *et al.* (2015).

We will focus in this paper on the three main units that compose the AMC: the Chah Gorbeh (CGC), Morghab (MC) and Ophiolitic (OC) complexes (Zanchi *et al.* 2015).

Quartzite-rich phyllites, micaschists and metabasites interlayered with thick metacarbonate layers (Figs 1, 2) form the CGC. Serpentinite lenses and layers occur in the southern part of the CGC.

The MC occurs to the north and east of the CGC. The MC has a more monotonous lithological composition, chiefly consisting of metapelites (phyllites and micaschists) with minor intercalations of quartzites, metabasites and thin marble layers. Regional folds with steep fold axes affected both the MC and CGC; this feature is particularly evident at the eastern end of the CGC (Fig. 1). To the south and southeast of the CGC an ‘ophiolitic’ complex (OC) occurs (Bagheri & Stampfli, 2008; Zanchi *et al.* 2015). This complex largely consists of serpentinites and partly serpentinitized harzburgites, where relics of the primary mineral assemblages and textures are scarcely preserved. In the central area of the OC some metabasite lenses have been observed (Fig. 1). Such lenses consist of metamorphosed basalts with well-preserved pillow structures. The OC is intensively folded with minor shear zones localized both along lithological contacts as well as within serpentinites.

The CGC, MC and OC units of the AMC are overthrust by a large thrust sheet of metacarbons, the Lakh Marble (Bagheri & Stampfli, 2008; Zanchi *et al.* 2015). These strongly recrystallized carbonates display an uneven distribution of deformation, with isoclinally folded areas coexisting with more preserved parts with sedimentary structures such as bedding, intraformational paraconglomerates (i.e. rich in matrix) and fossils. The age of the Lakh Marble is substantially unknown, although a late Palaeozoic age has been proposed based on indirect evidence (Bagheri & Stampfli, 2008). Recent re-examination of the presumed Lower Cambrian Archeocyatid faunas described by Russian authors in the past (Mel’nikov *et al.* 1986) resulted in the identification of the demosponge genus *Rankenella* (Kruse & Zhuralev, 2008) in the Kabudan Marble, which is a correlative of the Lakh Formation. These latter authors thus suggested a possible correlation with the Upper Cambrian Mila Formation of the Alborz Mountains, which implies a Gondwanan affinity for this unit.

Time constraints on the age of the high-pressure–low-temperature (HP–LT) metamorphism of the AMC are still lacking. A minimum age is provided by undeformed and non-metamorphosed trondhjemitic dykes and stocks that intruded the AMC (Torabi, 2012). Late Permian (Bagheri & Stampfli, 2008) to Sakmarian ages (Zanchi *et al.* 2015) have been provided for these intrusive rocks, suggesting that deformation and metamorphism of the AMC is Early Permian or older.

The AMC is currently interpreted as an allochthonous crustal fragment that was part of an accretionary wedge developed along the southern Eurasian margin, in the hangingwall of the Palaeo-Tethys subduction zone (Zanchi *et al.* 2015). In this interpretation, the formation of the AMC is considered to have preceded the collision of the Iran plate with Eurasia that led to the Cimmerian orogenic event.

3. Meso-structural aspects of the AMC

We summarize here the main structural features of the metabasite-bearing units of the AMC as observed in the field. For a more exhaustive description of the structural setting and evolution of the AMC see Zanchi *et al.* (2015).

3.a. Morghab Complex

The MC displays a complex structural pattern formed in response to superposed deformation events, the first two out of three associated with syn-metamorphic isoclinal folding. D_1 structures are now preserved at the mesoscale only as relicts within the S_2 regional foliation. Rootless fold hinges are somewhat visible in quartzites and quartz-rich schists, whereas D_1 -related structures are visible only at the microscale in metabasites. Mineral phase assemblages in textural equilibrium with D_1 structures point to HP–LT conditions during D_1 (Zanchi *et al.* 2015).

The D_2 deformation event is characterized by isoclinal folding developed both at the meso- and regional scale. The axial plane foliation, S_2 , of this fold system is the most pervasive fabric element within all the rock types that form the MC. Besides the S_2 foliation a well-developed stretching lineation defined by elongated quartz and chlorite has been frequently observed. The S_2 foliation is

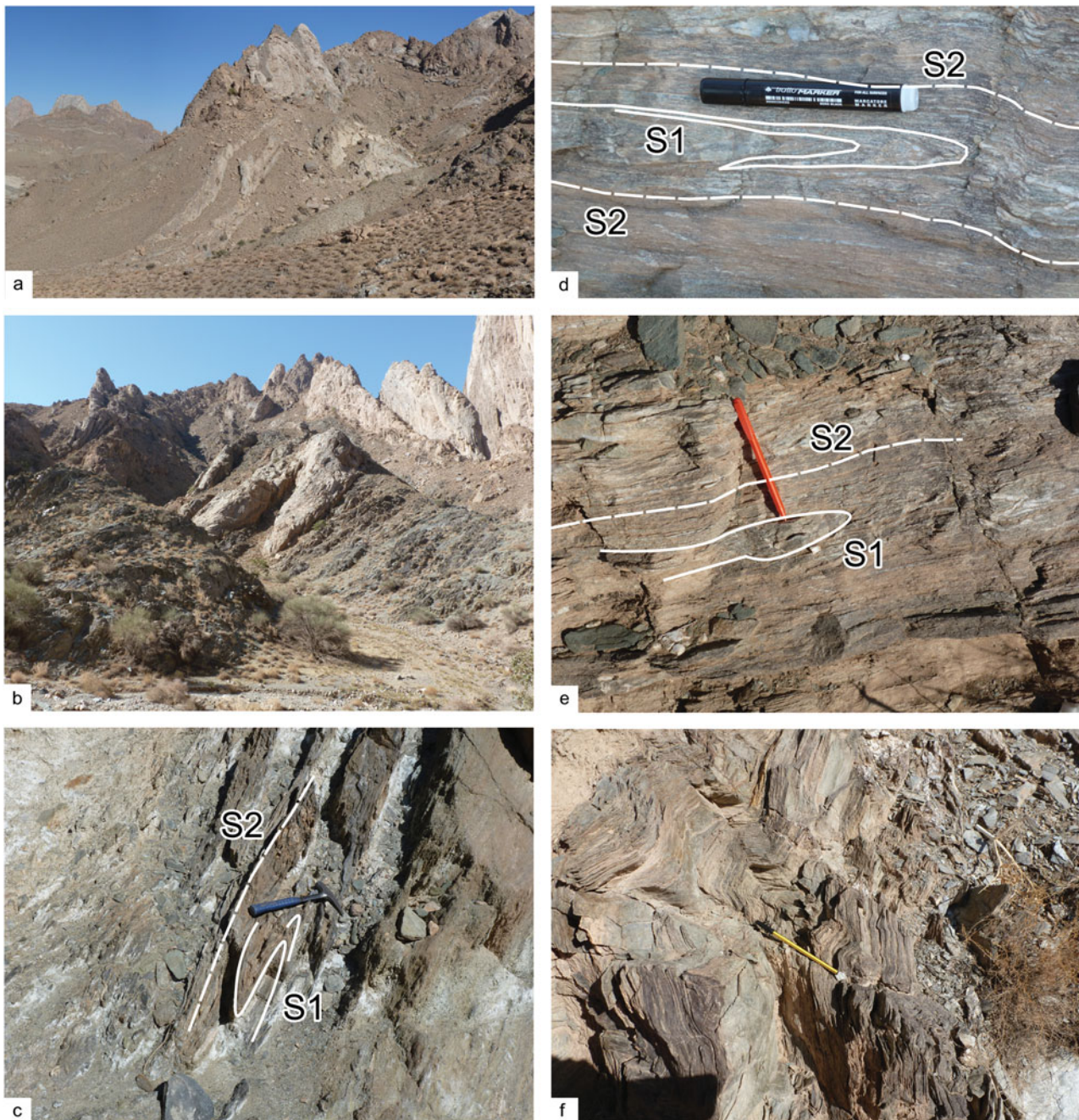


Figure 3. (Colour online) (a) Marble layers interleaved with metapelites and mafic schists of the CGC. (b) A fold hinge with a nearly vertical fold axis in the metacarbonates of the CGC. (c) S_1 relict foliation preserved within the regional S_2 foliation in paragneiss. Hammer for scale is 33 cm long. (d) S_1 relics within schists of the MC. Pen for scale is 14 cm long. (e) Superposed D_1 – D_2 folds in the MC rocks. Pen for scale is 15 cm long. (f) Open to medium-closed D_3 folds with an axial fracture cleavage. Pen for scale is 15 cm long.

concordant with lithological contacts within the MC and between the MC and adjoining units. Fold axes related to D_2 folds range from sub-horizontal to nearly vertical, suggesting that a successive deformation event affected the complex. This event, D_3 , is responsible for the development of medium-tight to closed folds observable both at the meso- and regional scale. D_3 folds deflecting the S_2 foliation and affecting the contact between the CGC and MC complexes are clearly reported in the geological-structural map of Figure 1 and characterize the present-day structural setting.

3.b. Chah Gorbah Complex

As in the MC the oldest recognized structures are poorly visible at the mesoscale. They are recognizable as relict S_1 foliation intrafolial in the dominant S_2 one (Fig. 3c, d). Rootless fold hinges seldom occur in metacarbonates and metapelites/metapsammities. The S_1 foliation is poorly visible at the mesoscale but clearly evident at the microscale where it is defined by a greenschist-facies mineral assemblage (Fig. 5).

The D_2 deformation event formed isoclinal folding associated with a pervasive axial plane foliation,

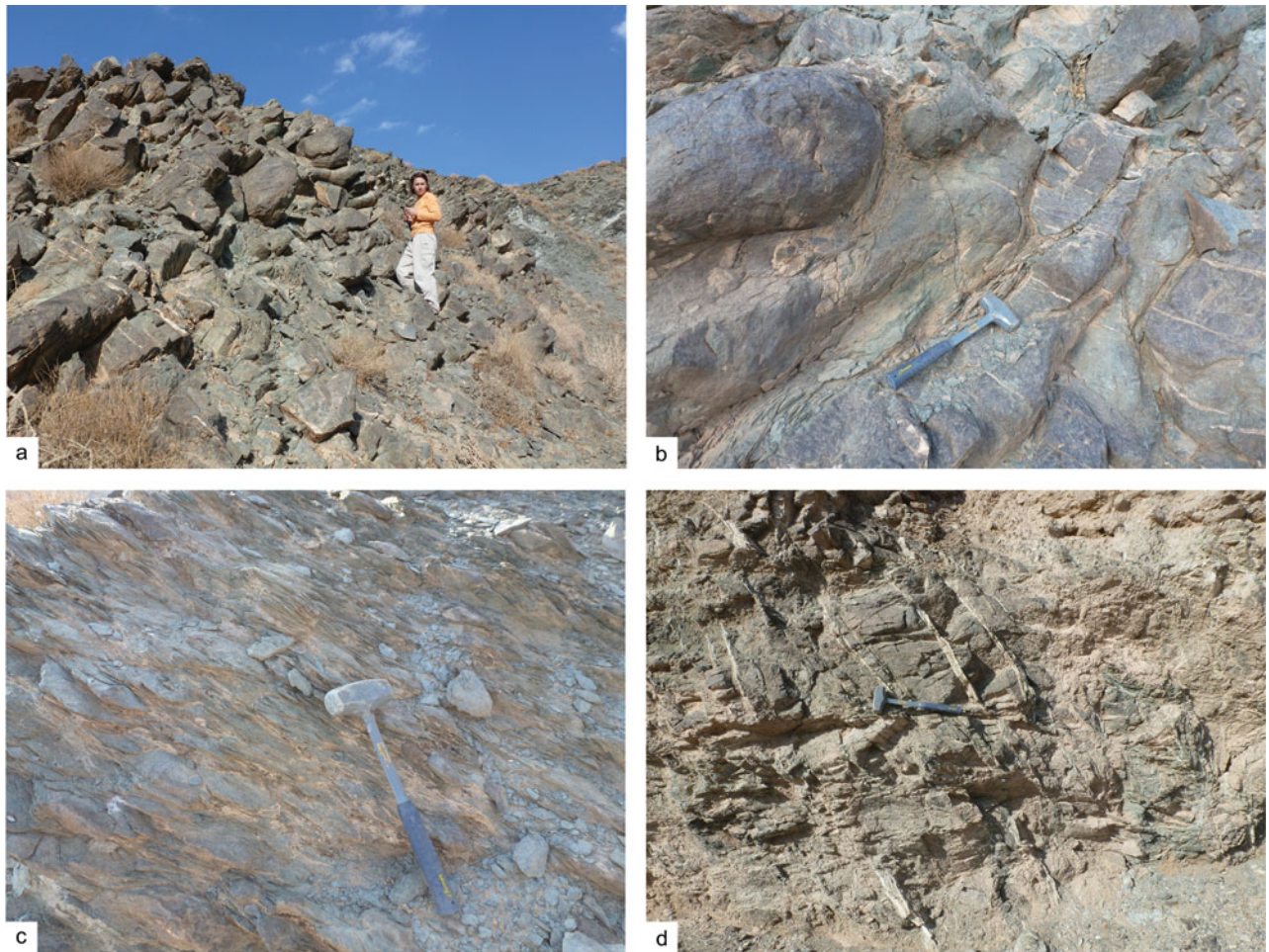


Figure 4. (Colour online) (a) Field aspect of pillow structure within meta-basalts of the OC; person for scale is *c.* 1.55–1.6 m tall. (b) Sheared domains developed at the rims of pillow. (c) Mylonitic foliation defined by blueschist-facies minerals at the contact between meta-basalts and serpentinites. (d) Calcite and quartz veins cross-cutting sheared serpentinites. Hammer for scale is 40 cm long.

S_2 , defined by Na-amphibole (Zanchi *et al.* 2015) that points to HP–LT metamorphism during the D_2 event. The different P – T conditions at which the regional foliation formed in the MC (greenschist facies) and CGC (blueschist facies) suggests that, even if the main foliations of both units are almost parallel to their contacts, they could not be related to a single deformation event that affected the MC and CGC together.

The contact between the CGC and serpentinites of the OC is marked by ductile shear zones (Fig. 2), sometimes with lenses of ophicalcites and impure marbles, where Na-amphibole is stable along the mylonitic foliation. This suggests that the MC and serpentinites were tectonically coupled at HP–LT conditions. In a few localities, in the southern part of the CGC, serpentinites are deformed by D_2 isoclinal folds together with rocks of the CGC. This observation suggests that the OC and serpentinites share a common tectonometamorphic evolution from the D_2 event onwards.

3.c. Ophiolitic Complex

We refer here to the whole complex of ultramafic rocks and blueschist-facies meta-basalts, the same that were

distinguished by Zanchi *et al.* (2015) into two units: ‘ultramafic rocks’ and ‘blueschist pillow meta-basalts’. The contacts between the ultramafic rocks and meta-basalts are always tectonic (Fig. 4c), so a direct correlation among structures observed in the two units is not feasible, justifying the distinction proposed by Zanchi *et al.* (2015).

Ultramafic rocks occur in two distinct structural settings: (1) as tectonic slices within the southern part of the CGC, as previously described; (2) as a continuous unit, forming complex imbricated thrust sheets, in a lower structural position with respect to the CGC (Fig. 2). Peridotites of type (1) are almost completely serpentinized and intensively sheared with foliations subparallel to the S_2 of the CGC and to tectonic contacts. Peridotites of type (2) show a patchy distribution of deformation with isolated lenses conserving a massive texture with preserved olivine, orthopyroxene and spinel crystals. This mineral assemblage indicates a harzburgitic composition for the ultramafic rocks of the AMC. Such massive domains are wrapped by sheared domains where a pervasive schistosity is associated with an almost complete serpentinization of harzburgites.

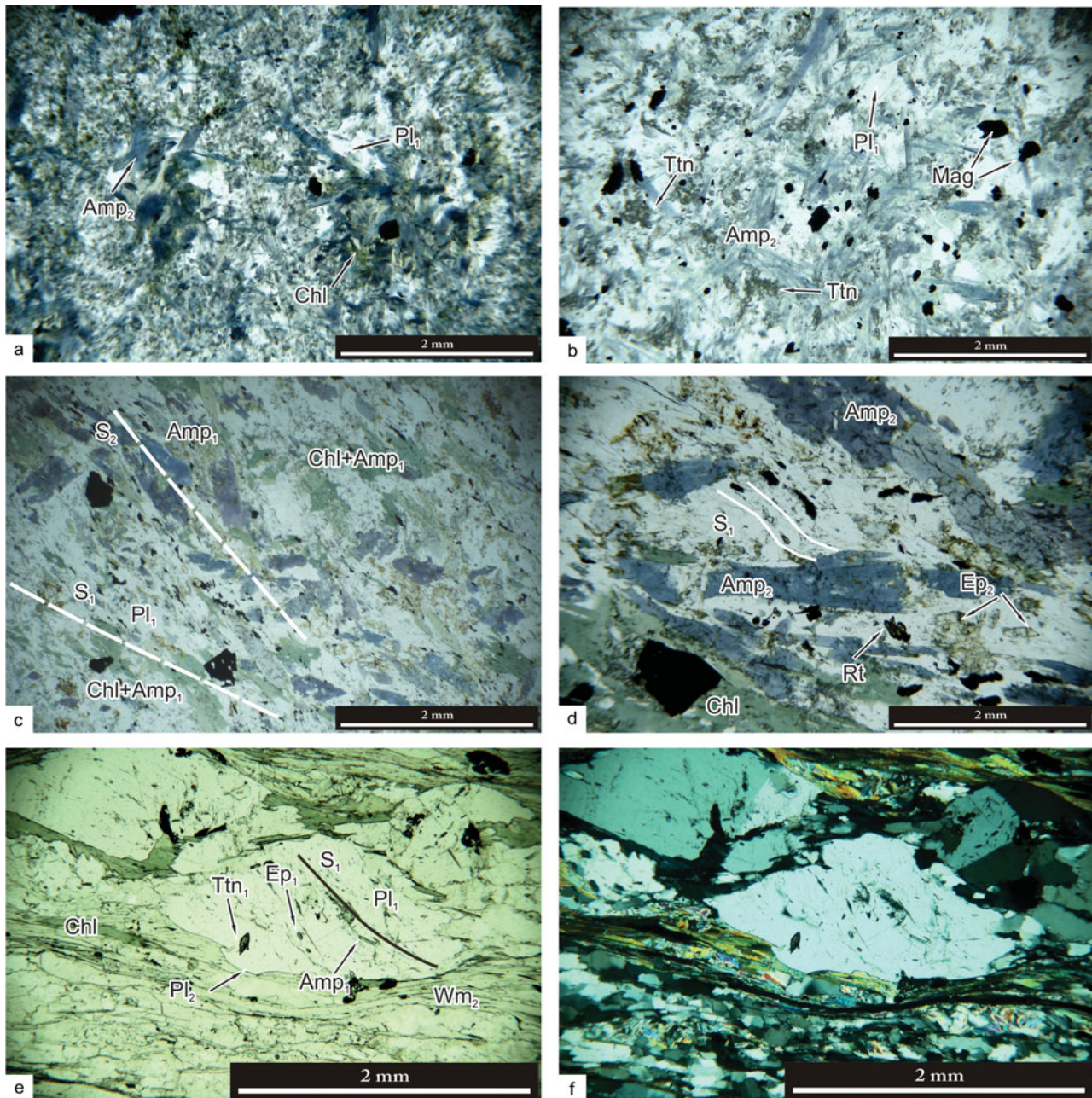


Figure 5. (Colour online) Microstructural features of mafic schists. (a, b) Static growth of blue amphibole (Amp_2), magnetite and titanite (Ttn_2) on existing greenschist-facies assemblage in meta-basalts. (c, d) Syn-kinematic Na-amphibole (Amp_2) and epidote (Ep_2) aligned parallel to S_2 within mafic schists of the CGC. Relics of a greenschist-facies S_1 foliation are best preserved within plagioclase porphyroblasts. (e, f) Blueschist-facies phase assemblage aligned defining the internal foliation of plagioclase porphyroblasts (Pl_2) in retrogressed blueschists of the MC.

Meta-basalts with well-preserved pillow structures (Fig. 4a, b) occur ESE of Chah Derakhtak (Fig. 1). Such slices form part of a complex S-verging thrust stack also involving serpentinites and ophiolites (Sharkovski, Susov & Krivyakin, 1984; Zanchi *et al.* 2009, 2015). Except within shear zones, where pillows are partially to almost completely transposed (Fig. 4c), the meta-basalts are substantially undeformed. A poorly defined foliation is distinguishable only at the microscale, defined by greenschist-facies mineral assemblage (see next section).

4. Microstructural and metamorphic evolution

Microstructural analyses on selected samples of mafic rocks from the three tectonic units were performed to decipher the deformation–metamorphism relationships in each unit. The multi-stage structural evolution reconstructed at the mesoscale has also been recognized at the microscale. A brief overview of the chemical composition of key minerals occurring at distinct microstructural positions is provided here, whereas the reader is referred to the next section for a complete description of the AMC rocks' mineral

chemistry. Mineral abbreviations used in the text are reported in Table 1.

4.a. Morghab Complex

The mineralogy of mafic schists of the MC is made of (Table 1): amphibole, plagioclase, epidote, chlorite, white mica, titanite, quartz, magnetite and apatite. Secondary calcite occurring in veins and microcracks post-dating the main foliation has been observed in some samples.

Metabasites of the MC are fine grained with the main fabric element at the microscale represented by a well-developed foliation. Cores of epidote (Ep₂) and albitic plagioclase (Pl₁) porphyroblasts partially pre-date the main foliation. Aligned inclusion trails have been observed both within Pl₂ and Ep₂. They consist of blue Na-rich amphibole (Amp₁), white mica (Wm₁), titanite (Ttn₁), quartz, albite (Pl₁) and epidote (Ep₁). Pl₁ and Ep₁ inclusions occur within Ep₂ and Pl₂, respectively. The main foliation, which corresponds to the regional S₂ foliation as recognized by field structural analysis, wraps around plagioclase and epidote porphyroblast cores. The outer rims of both Ep₂ and Pl₂ seem to overgrow the foliation, so we consider the porphyroblast rims to be syn- to post-kinematic with respect to S₂. The S₂ foliation is defined by the shape preferred orientation (SPO) of Amp₂ + Chl + Wm₂ + Ttn₂. Amp₂ occurs in the form of tiny to fine-grained crystals with a subidiomorphic to idiomorphic (prismatic) habit. They frequently contain inclusions of quartz, chlorite and plagioclase. Ttn₂ forms trails of (sub)millimetric (max. 1.5 mm) crystals aligned parallel to S₂. Ttn₂ crystals always have the typical lozenge-shaped prismatic habit of titanite with the major axis elongated parallel to the S₂ foliation. Both Ttn₂ and Amp₂ have been observed as inclusions in Ep₂ porphyroblasts rims, suggesting that epidote crystal growth outlasted the D₂ deformation event. A colour zoning is frequently observed in Amp₂: microchemical analyses (see next section) highlighted a Na-increase from the core to the rim of Amp₂ crystals. A similar compositional zoning also occurs in Ep₂ porphyroblasts, with rims enriched in Fe³⁺ with respect to the cores. This suggests a pressure increase during the late stages of the D₂ deformation event. Amp₂ crystals also occur as inclusions within Ep₂ rims.

Summarizing the metamorphic evolution individuated for the mafic schists of the MC we can define three successive parageneses: (i) Blueschist facies (pre-S₂): Amp₁ + Wm₁ + Ttn₁ + Ep₁ + Pl₁ + Qtz; (ii) Greenschist facies (syn-S₂): Amp₂ (core) + Chl + Wm₂ + Ep₂ (core) + Pl₂ + Ttn₂ + Qtz; (iii) Greenschist with *P* increase (late-, post-S₂): Amp₂(rim) + Ep₂(rim).

4.b. Chah Gorbbeh Complex

The mineralogy of metabasites of the CGC consists of: amphibole, plagioclase, chlorite, white mica, epidote,

Table 1. Sample descriptions and locations

Sample	Tectonic unit	Rock type	Mineralogy													Coordinates		
			Qtz	Pl	Wm	Ep	Cc	Chl	Rt	Ttn	Amp	Mt	ox	Ap	Zr	Pyr	Latitude (N)	Longitude (E)
AK33A	Pillow meta-basalts	Blueschist	x	x	x	x	x	x	x	x	x	x	x	x	x	x	33° 23' 41"	53° 45' 10"
AK33B	Pillow meta-basalts	Blueschist	x	x	x	x	x	x	x	x	x	x	x	x	x	x	33° 23' 41"	53° 45' 10"
AK36	Pillow meta-basalts	Blueschist	x	x	x	x	x	x	x	x	x	x	x	x	x	x	33° 23' 36"	53° 45' 07"
I13-06	Chah Gorbbeh	Blueschist	x	x	x	x	x	x	x	x	x	x	x	x	x	x	33° 26' 02"	53° 45' 11"
I13-09	Chah Gorbbeh	Blueschist	x	x	x	x	x	x	x	x	x	x	x	x	x	x	33° 25' 53"	53° 44' 48"
I13-11	Chah Gorbbeh	Blueschist	x	x	x	x	x	x	x	x	x	x	x	x	x	x	33° 25' 51"	53° 44' 43"
AK14A	Morghab	Greenschist (Blueschist relics)	x	x	x	x	x	x	x	x	x	x	x	x	x	x	33° 26' 36"	53° 45' 45"
AK19B	Morghab	Greenschist (Blueschist relics)	x	x	x	x	x*	x	x	x	x	x	x	x	x	x	33° 26' 03"	53° 43' 19"

Notes: Mineral abbreviations. Amp – amphibole; Ap – apatite; Cc – calcite; Chl – chlorite; Ep – epidote; Mt – magnetite; Ol – olivine; ox – Fe-Ti oxides; Pl – plagioclase; Pyr – pyrite; Qtz – quartz; Rt – rutile; Ttn – titanite; Wm – white mica; Zr – zircon. X* – secondary minerals.

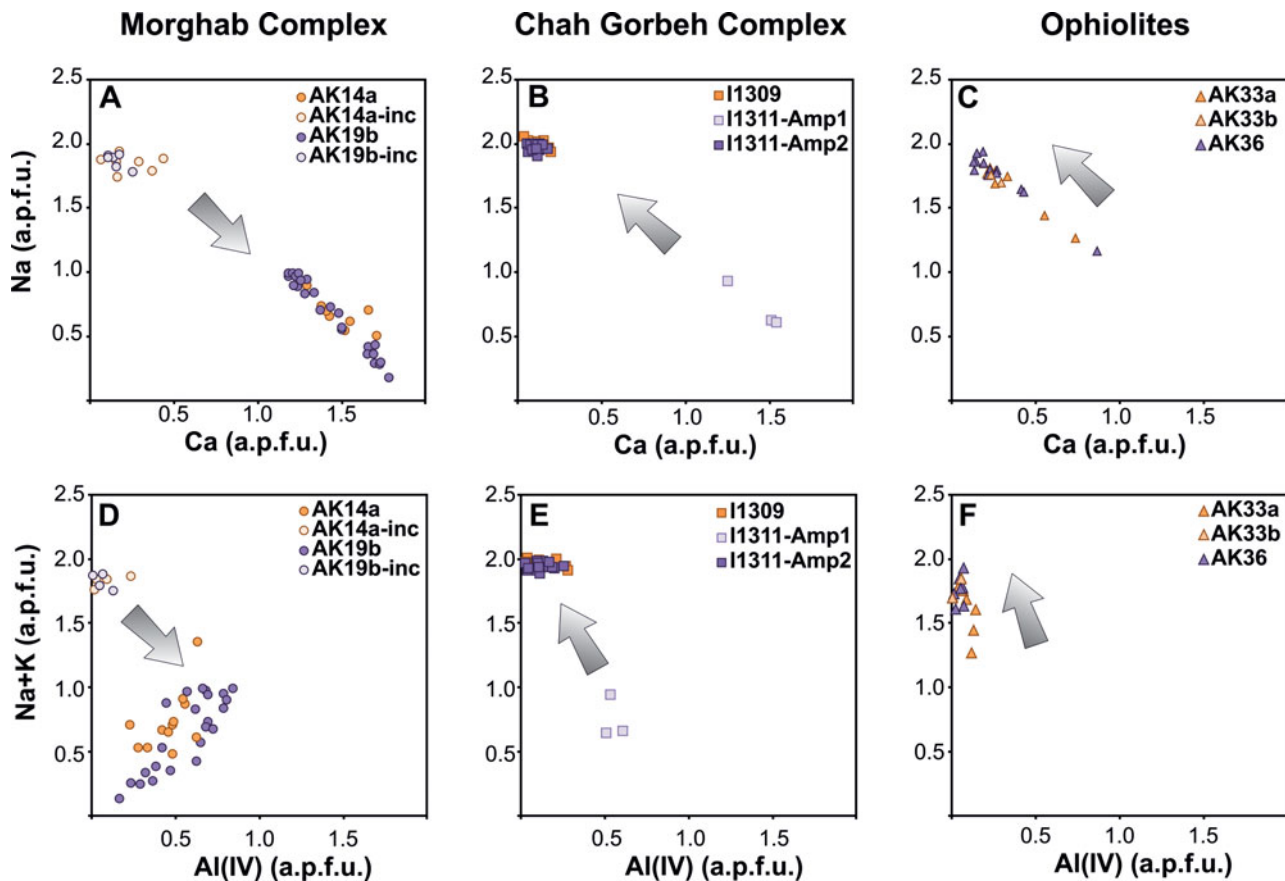


Figure 6. (Colour online) Representative amphibole compositions of mafic schists for the CGC, MC and OC. Arrows indicate the evolution direction (old to young) as recognized by microstructural analyses.

quartz, titanite, rutile, calcite, apatite, zircon and pyrite (Table 1).

The textural features of the mafic schists from the CGC closely resemble the ones described for the rocks of the MC. The development of a primary foliation is preceded by plagioclase (Pl_1) and epidote (Ep_1) porphyroblast growth, with a peculiar mineral phase assemblage of oriented inclusions. However, the metamorphic evolution is discordant, as we will describe below.

An internal foliation (S_1) made by the preferred orientation of $Ttn_1 + Pl_1 + Qtz + Amp_1$ inclusions is highlighted within Pl_1 and Ep_1 porphyroblasts. Amp_1 is actinolitic hornblende (Fig. 6; Table 3), suggesting equilibration at relatively low P under greenschist-facies conditions. The main foliation (S_2) is defined by the SPO of $Chl + Ab + Wm_1 + Ep_2 + Rt + Amp_2$. Blue-coloured Amp_2 is ferroglaucophane (Table 3) in composition and displays clear cores without inclusions, coupled with inclusion-rich rims, where Wm_1 , Chl and Ep_2 aligned parallel to S_2 occur. Ep_2 is Fe-enriched (Fig. 6) with respect to Ep_1 , pointing to a P increase from the D_1 to D_2 deformation/metamorphic event. Tiny magnetite crystals occur as trails aligned parallel to S_2 . Rutile, usually overgrown by rims of titanite (Ttn_2), has also been observed only outside Pl_1 and Ep_1 porphyroblasts. Therefore, its growth and incomplete substitution by Ttn_2 could be assigned to the syn- to post- S_2 metamorphic stage.

Two main metamorphic stages can be defined for the CGC: (i) Greenschist facies (pre- S_2): $Ep_1 + Pl_1 + Ttn_1 + Amp_1 + Wm_1 + Qtz$; (ii) Blueschist facies (syn- to post- S_2): $Amp_2 + Chl + Ep_2 + Pl_2 + Mt + Wm_1 + Rt$ (Ttn_2)

4.c. Ophiolitic Complex (meta-basalts)

As described in Section 3.c, meta-basalts crop out in the southern area of the AMC in tectonic contact with serpentinized ultramafic rocks (Figs 1, 2). As observed in outcrops, where the primary pillow structures are completely preserved, the meta-basalts also show little deformation at the microscale. The complete mineralogy is defined by: amphibole, plagioclase, chlorite, epidote, white mica, magnetite, apatite and Fe–Ti oxides.

Meta-basalts are fine grained with a very poorly defined foliation (S_1) made by the SPO of $Pl_1 + Chl + Amp_1 + Ep_1 + Ttn_1$, with Amp_1 displaying an actinolitic composition. This weak foliation is overprinted by the static growth of prismatic Na-rich blue amphibole (Amp_2) and aggregates of titanite crystals (Ttn_2) that show no evidence of deformation. Besides their occurrence as relatively large (up to 2 mm) prismatic crystals (Fig. 5), Amp_2 has also been observed to grow as thin coronae around $Chl + Amp_1$ sites (Fig. 5). Based on microstructural analysis, the meta-pillow basalts show a prograde metamorphic

evolution, with a greenschist-facies foliation overprinted by the static growth of a HP–LT blueschist-facies phase assemblage as summarized below:

(i) Greenschist (syn- S_1): Amp₁ + Pl₁ + Chl + Wm₁ + Ep₁ + Ttn₁ + Qtz; (ii) Blueschist (post- S_1): Amp₂ + Ttn₂ + Wm₂.

5. Mineral chemistry and P – T – d – t paths

5.a. Methods

Textural and mineralogical features were inspected on polished thin-sections using back-scattered electron (BSE) and secondary electron images and characterized by electron microprobe analyses. Analyses were performed at the Earth Science Department of the University of Milano on a Jeol JXA 8200 Superprobe equipped with five wavelength-dispersive spectrometers (WDS). Analyses were conducted with a *c.* 1 μm beam diameter at conditions of 15 kV and 5 nA of probe current. Natural silicates and oxides were used as standards. All standards were calibrated within 0.5% at one standard deviation. Raw data were corrected using a Phi-Rho-Z quantitative analysis program. Major elements and recalculated structural formulae are reported in Tables 2, 3 and 4.

Whole-rock analysis for major elements, used for the isochemical P – T pseudosection (see below), was determined at the ACME Analytical Laboratories Ltd in Vancouver (Canada). Total abundances of the major oxides were obtained by ICP-ES (inductively coupled plasma emission spectroscopy) following a LiBO₂ fusion and dilute nitric digestion for major oxides. Analytical errors are within 2%.

The FeO weight % on total FeO* has been determined for the AK14 sample by titration following the Wilson method (Wilson, 1955; Yokoyama & Nakamura, 2002 and references therein) at the Department of Earth and Environmental Sciences, University of Milano Bicocca.

5.b. Results

5.b.1. Morghab Complex

Porphyroblastic epidote and plagioclase preserve a relict paragenesis composed by Amp₁ + Wm₁ + Ttn₁ + Ep₁ + Pl₁ + Qtz (fig. 12b in Zanchi *et al.* 2015). Micron-sized Amp₁ is an alkali-amphibole (NaB > 1.50) and corresponds to a glaucophane (Table 2), while Amp₂ along the main foliation is calcic to sodic-calcic (Ca + Na) B > 1, 0.5 < NaB < 1.5 and variable CaB. This mainly corresponds to actinolite and magnesiokatophorite and shows a slight zoning from core to rim, with a decrease in CaO, complementary to a slight increase in Na₂O (Table 2; Fig. 6d). In addition epidote shows a strong compositional variation. Ep₁ included in albite porphyroblasts show higher FeO* contents with respect to the cores of Ep₂, which in turn is characterized by a compositional zoning with the rim enriched in

FeO* with respect to the core (Table 2). This prograde zoning is likely related to the core-to-rim increase in Na₂O recorded by Amp₂. Both white micas, Wm₁ included in porphyroblastic albite and Wm₂ along the S_2 foliation, show a moderate celadonic content, in the range of 3.35–3.50 atoms per formula unit (apfu) (Table 2). Finally, plagioclase is mainly albite and does not show any anorthite substitution in both generations.

5.b.2. Chah Gorbeh Complex

Different from the Morghab mafic rocks, these samples show a prograde evolution from greenschist-facies to a blueschist-facies overprint, as recorded also by a different mineral composition. The main foliation is in fact characterized by rare actinolitic amphibole and abundant alkali-amphiboles (NaB > 1.50) showing homogeneous composition with the highest Na contents (up to 2.03 apfu, Table 3). They are classified as ferroglaucophane. In a Na v. Ca (Fig. 6a, b) and (Na + K) v. Al^(IV) diagram (Fig. 6d, e) they show a trend similar to that of amphiboles from the MC with the difference that this is prograde. Na and Na + K become enriched with respect to Ca and Al^(IV), respectively, from Amp₁ to Amp₂ as indicated by the grey arrow. Glaucophane is characterized by inclusion-rich rims. Such inclusions consist of the same mineral phases as those crystallized along the main foliation (Chl, Ab, Wm, Ep and rutile with Ttn coronae). In some samples, epidote along the S_2 foliation also shows a poikiloblastic texture and includes quartz, albite and titanite. Such epidotes are enriched in FeO*, in agreement with equilibration with glaucophane (Table 3) and do not show the strong iron variability as recorded by epidotes of the mafic rocks from the MC. Both white micas, Wm₁ included in glaucophane rims and porphyroblastic albite, and Wm₂ along the S_2 foliation, show a moderate celadonic content, in the range of 3.30–3.40 apfu (Table 3). Again, plagioclase is mainly albite and does not show any anorthite substitution.

5.b.3. Ophiolitic Complex (meta-basalts)

Meta-basalts from the OC show a very weak foliation made of Pl₁ + Chl + Amp₁ + Ep₁ + Ttn₁, with Amp₁ displaying an actinolitic composition, overprinted by the static growth of Amp₂ and aggregates of Ttn₂. Amp₂ occur both as fine-grained aggregates and as millimetre-sized prismatic crystals. As shown in Table 4, fine-grained Amp₂ has a variable composition, locally between alkali to sodic-calcic amphiboles (NaB from 1.29 to 1.69 apfu). Coarse Amp₂ is instead homogeneous in composition and corresponds to a magnesioriebeckite. It shows slightly lower Na content with respect to alkali-amphibole occurring in the Chah Gorbeh mafic rocks (Table 4; Fig. 6c, f). Some coarse white micas appear in microstructural equilibrium with Amp₂ and are characterized by a higher celadonic substitution, up to 3.55 (Table 4), with

Table 2. Average composition of major elements (ox. wt%) and of recalculated structural formulae of minerals composing mafic rocks from the Morghab Complex (numbers in brackets are standard deviations)

Sample Mineral Microstructural position No. analyses	Amphibole						Epidote					Titanite		Plagioclase				Phengite			
	AK14A			AK19B			AK14A			AK19B		AK14A		AK19B		AK14A		AK19B		AK19B	
	Amp ₁ Inc in Ep2	Amp ₂ Core	Amp ₂ Rim	Amp ₁ Inc in Ep2	Amp ₂ Core	Amp ₂ Rim	Ep ₁ Inc in Ab	Ep ₂ Core	Ep ₂ Rim	Ep ₂ Core	Ep ₂ Rim	Ttn ₁ Inc in Ep2	Ttn ₂ 4	Ab Porph Core	Ab Porph Rim	Ab ₂ 1	Ab Porph 2	Wm ₁ Inc in Ab	Wm ₂ 8	Wm ₁ Inc in Ab	Chlorite Chl 2
	9	5	5	7	12	14	2	4	6	4	4	2	4	1	1	1	2	3	8	3	
SiO ₂	55.79 (0.78)	51.74 (1.11)	50.83 (0.99)	55.85 (0.48)	51.40 (1.81)	49.44 (1.06)	37.96 (0.35)	38.23 (0.25)	37.49 (0.26)	37.92 (0.19)	37.18 (0.44)	30.78 (0.37)	30.34 (0.08)	69.21	68.63	69.33	68.54 (0.52)	51.41 (0.78)	52.29 (1.99)	51.29 (1.35)	26.54 (0.52)
TiO ₂	0.03 (0.03)	0.50 (0.96)	0.06 (0.02)	0.03 (0.02)	0.07 (0.05)	0.12 (0.05)	0.06 (0.00)	0.05 (0.02)	0.04 (0.03)	0.06 (0.03)	0.04 (0.04)	35.36 (2.59)	38.03 (0.29)	0.01	0.00	0.00	0.00 (0.00)	0.07 (0.02)	0.14 (0.11)	0.07 (0.03)	0.08 (0.06)
Al ₂ O ₃	8.58 (1.10)	4.02 (1.46)	4.55 (0.93)	7.99 (0.89)	3.75 (1.47)	6.44 (0.77)	24.47 (2.54)	26.55 (0.27)	22.63 (0.24)	25.23 (0.73)	23.20 (1.31)	1.88 (1.33)	1.01 (0.20)	19.88	19.76	20.00	19.74 (0.21)	28.44 (1.84)	25.65 (1.55)	30.47 (2.29)	19.62 (0.25)
Cr ₂ O ₃	0.01 (0.01)	0.01 (0.02)	0.02 (0.03)	0.00 (0.01)	0.03 (0.03)	0.01 (0.02)	0.03 (0.04)	0.02 (0.03)	0.00 (0.00)	0.02 (0.03)	0.03 (0.03)	0.06 (0.01)	0.01 (0.02)	0.01	0.02	0.02	0.02 (0.03)	0.02 (0.04)	0.01 (0.01)	0.03 (0.05)	0.00 (0.00)
FeO*	17.82 (0.52)	17.06 (0.94)	19.41 (1.17)	16.91 (0.76)	16.17 (1.82)	18.44 (0.72)	10.68 (3.10)	8.61 (0.25)	13.25 (0.37)	10.26 (0.96)	12.69 (1.83)	1.17 (0.63)	0.47 (0.15)	0.01	0.09	0.14	0.09 (0.11)	4.04 (0.26)	5.20 (1.67)	3.02 (0.39)	25.92 (0.31)
MgO	6.65 (0.36)	11.34 (0.98)	10.12 (0.87)	7.91 (0.27)	12.73 (1.41)	10.44 (0.63)	0.01 (0.02)	0.02 (0.01)	0.01 (0.01)	0.01 (0.01)	0.03 (0.01)	0.00 (0.00)	0.01 (0.01)	0.00	0.00	0.01	0.01 (0.00)	2.67 (1.50)	3.10 (0.39)	2.00 (0.63)	15.79 (0.30)
MnO	0.18 (0.05)	0.28 (0.02)	0.32 (0.04)	0.17 (0.05)	0.35 (0.06)	0.36 (0.03)	0.17 (0.09)	0.14 (0.04)	0.21 (0.04)	0.23 (0.08)	0.20 (0.08)	0.03 (0.02)	0.03 (0.03)	0.02	0.00	0.00	0.00 (0.00)	0.02 (0.02)	0.04 (0.04)	0.02 (0.03)	0.42 (0.09)
CaO	1.66 (0.88)	10.01 (0.76)	8.73 (0.66)	1.00 (0.32)	10.32 (0.89)	7.90 (0.41)	23.03 (0.44)	23.37 (0.09)	22.56 (0.11)	23.16 (0.24)	22.75 (0.13)	28.02 (0.16)	28.19 (0.17)	0.06	0.05	0.08	0.05 (0.01)	0.09 (0.09)	0.07 (0.04)	0.01 (0.01)	0.04 (0.01)
Na ₂ O	6.70 (0.28)	1.89 (0.44)	2.56 (0.50)	6.77 (0.17)	1.50 (0.57)	3.17 (0.26)	0.01 (0.01)	0.00 (0.00)	0.01 (0.01)	0.01 (0.00)	0.01 (0.02)	0.01 (0.02)	0.02 (0.02)	11.87	11.96	11.50	11.47 (0.04)	0.28 (0.05)	0.15 (0.05)	0.38 (0.10)	0.01 (0.01)
K ₂ O	0.02 (0.02)	0.17 (0.05)	0.21 (0.04)	0.01 (0.01)	0.15 (0.07)	0.22 (0.04)	0.00 (0.00)	0.00 (0.00)	0.00 (0.01)	0.00 (0.00)	0.00 (0.00)	0.01 (0.01)	0.02 (0.01)	0.04	0.05	0.04	0.05 (0.00)	9.43 (0.23)	9.74 (0.21)	9.78 (0.16)	0.01 (0.01)
Total	97.45 (0.43)	97.01 (0.45)	96.81 (0.41)	97.36 (1.29)	96.56 (0.77)	96.80 (0.79)	96.42 (0.21)	96.99 (0.26)	96.21 (0.25)	96.90 (0.13)	96.13 (0.32)	97.32 (0.14)	98.14 (0.38)	101.11	100.56	101.12	99.96 (0.26)	96.47 (0.95)	96.40 (1.30)	97.06 (0.18)	88.40 (0.23)
Si	7.94 (0.11)	7.59 (0.15)	7.54 (0.11)	7.98 (0.06)	7.56 (0.19)	7.34 (0.12)	3.02 (0.01)	3.00 (0.01)	3.01 (0.02)	2.99 (0.02)	2.98 (0.02)	1.02 (0.01)	1.00 (0.00)	2.99	2.98	3.00	3.00 (0.02)	3.39 (0.03)	3.47 (0.07)	3.34 (0.09)	2.79 (0.05)
Ti	0.00 (0.00)	0.05 (0.11)	0.01 (0.00)	0.00 (0.00)	0.01 (0.01)	0.01 (0.01)	0.00 (0.00)	0.00 (0.00)	0.00 (0.00)	0.00 (0.00)	0.00 (0.00)	0.00 (0.07)	0.88 (0.01)	0.94	0.00	0.00	0.00 (0.00)	0.00 (0.00)	0.01 (0.01)	0.00 (0.00)	0.01 (0.01)
Al	1.44 (0.18)	0.70 (0.25)	0.80 (0.17)	1.35 (0.15)	0.65 (0.26)	1.13 (0.14)	2.29 (0.21)	2.46 (0.02)	2.14 (0.02)	2.35 (0.06)	2.19 (0.11)	0.07 (0.05)	0.04 (0.01)	1.01	1.01	1.02	1.02 (0.01)	2.21 (0.14)	2.01 (0.11)	2.34 (0.17)	2.43 (0.04)
Cr	0.00 (0.00)	0.00 (0.00)	0.00 (0.00)	0.00 (0.00)	0.00 (0.00)	0.00 (0.00)	0.00 (0.00)	0.00 (0.00)	0.00 (0.00)	0.00 (0.00)	0.00 (0.00)	0.00 (0.00)	0.00 (0.00)	0.00	0.00	0.00	0.00 (0.00)	0.00 (0.00)	0.00 (0.00)	0.00 (0.00)	0.00 (0.00)
Fe*	2.12 (0.07)	2.09 (0.12)	2.41 (0.15)	2.02 (0.09)	1.99 (0.24)	2.29 (0.10)	0.71 (0.21)	0.56 (0.02)	0.89 (0.02)	0.68 (0.07)	0.85 (0.13)	0.03 (0.02)	0.01 (0.00)	0.00	0.00	0.00	0.00 (0.00)	0.22 (0.02)	0.29 (0.10)	0.16 (0.02)	2.28 (0.04)
Mg	1.41 (0.08)	2.48 (0.20)	2.24 (0.18)	1.68 (0.06)	2.79 (0.28)	2.31 (0.13)	0.00 (0.00)	0.00 (0.00)	0.00 (0.00)	0.00 (0.00)	0.00 (0.00)	0.00 (0.00)	0.00 (0.00)	0.00	0.00	0.00	0.00 (0.00)	0.26 (0.15)	0.31 (0.04)	0.19 (0.06)	2.47 (0.04)
Mn	0.02 (0.01)	0.03 (0.00)	0.04 (0.00)	0.02 (0.01)	0.04 (0.01)	0.05 (0.00)	0.01 (0.01)	0.01 (0.00)	0.01 (0.00)	0.02 (0.01)	0.01 (0.01)	0.00 (0.00)	0.00 (0.00)	0.00	0.00	0.00	0.00 (0.00)	0.00 (0.00)	0.00 (0.00)	0.00 (0.00)	0.04 (0.01)
Ca	0.25 (0.13)	1.57 (0.11)	1.39 (0.10)	0.15 (0.05)	1.63 (0.13)	1.26 (0.07)	1.96 (0.01)	1.96 (0.01)	1.94 (0.01)	1.96 (0.01)	1.95 (0.00)	0.99 (0.00)	1.00 (0.00)	0.00	0.00	0.00	0.00 (0.00)	0.01 (0.01)	0.01 (0.00)	0.00 (0.00)	0.00 (0.00)
Na	1.85 (0.07)	0.54 (0.13)	0.74 (0.15)	1.87 (0.05)	0.43 (0.17)	0.91 (0.08)	0.00 (0.00)	0.00 (0.00)	0.00 (0.00)	0.00 (0.00)	0.00 (0.00)	0.00 (0.00)	0.00 (0.00)	0.99	1.01	0.97	0.97 (0.00)	0.04 (0.01)	0.02 (0.01)	0.05 (0.01)	0.00 (0.00)
K	0.00 (0.00)	0.03 (0.01)	0.04 (0.01)	0.00 (0.00)	0.03 (0.01)	0.04 (0.01)	0.00 (0.00)	0.00 (0.00)	0.00 (0.00)	0.00 (0.00)	0.00 (0.00)	0.00 (0.00)	0.00 (0.00)	0.00	0.00	0.00	0.00 (0.00)	0.79 (0.02)	0.83 (0.02)	0.81 (0.01)	0.00 (0.00)
Total	15.05 (0.02)	15.09 (0.08)	15.20 (0.09)	15.08 (0.04)	15.13 (0.11)	15.33 (0.05)	8.00 (0.00)	8.00 (0.00)	8.00 (0.00)	8.00 (0.00)	8.00 (0.00)	3.00 (0.00)	3.00 (0.00)	5.00	5.00	5.00	5.00 (0.00)	6.92 (0.03)	6.94 (0.05)	6.91 (0.00)	10.87 (0.00)

Table 3. Average composition of major elements (ox. wt%) and of recalculated structural formulae of minerals composing mafic rocks from the Chah Gorbah Complex (numbers in brackets are standard deviations)

Sample Mineral Microstructural position No. analyses	Amphibole							Epidote						Titanite		Plagioclase					Phengite					Chlorite		
	I1309			I1311				I1309			I1311			I1309		I1309			I1311		I1309			I1311		I1309		
	Amp ₂ Core	Amp ₂ Int	Amp ₂ Rim	Amp ₁	Amp ₂ Core	Amp ₂ Int	Amp ₂ Rim	Ep ₁ Inc in Ab	Ep ₂ Core	Ep ₂ Int	Ep ₂ Rim	Ep ₂ Core	Ep ₂ Int	Ep ₂ Rim	Ttn ₂ Core	Ttn ₂ Rim	Ab Porph Core	Ab Porph Int	Ab Porph Rim	Ab Porph Core	Ab Porph Rim	Wm ₁ Inc in Amp ₂	Wm ₂ Core	Wm ₂ Rim	Wm ₁ Inc in Ab	Wm ₂	Chl	
SiO ₂	55.91 (0.18)	55.24 (1.19)	56.24 (0.58)	50.66 (0.51)	55.29 (1.01)	55.75 (0.72)	54.95 (1.01)	38.07 (0.06)	37.21 (0.04)	37.79 (0.45)	37.92 (0.34)	37.83 (0.04)	38.26 (0.18)	38.27 (0.03)	30.91 (0.06)	31.05 (0.06)	68.86 (0.30)	69.08 (0.24)	70.09 (1.55)	69.29 (0.51)	69.33 (0.29)	51.69 (0.12)	51.42 (0.53)	51.21 (0.45)	51.45 (1.27)	50.78 (0.46)	26.10 (0.57)	
TiO ₂	0.11 (0.04)	0.12 (0.09)	0.08 (0.03)	0.06 (0.05)	0.17 (0.08)	0.13 (0.06)	0.18 (0.06)	0.10 (0.03)	0.22 (0.14)	0.25 (0.04)	0.36 (0.38)	0.10 (0.03)	0.09 (0.03)	0.03 (0.03)	35.71 (0.06)	35.66 (0.06)	0.03 (0.04)	0.01 (0.01)	0.04 (0.04)	0.02 (0.00)	0.02 (0.02)	0.25 (0.08)	0.24 (0.07)	0.20 (0.06)	0.20 (0.09)	0.24 (0.07)	0.29 (0.03)	
Al ₂ O ₃	8.20 (0.35)	8.58 (0.49)	8.22 (0.49)	4.58 (0.63)	7.95 (0.71)	8.15 (0.55)	7.90 (0.43)	24.43 (0.30)	21.88 (0.78)	23.64 (0.69)	24.19 (0.43)	23.76 (0.30)	22.49 (0.30)	23.14 (0.30)	2.62 (0.06)	2.60 (0.06)	19.86 (0.38)	19.86 (0.01)	20.26 (0.23)	19.90 (0.15)	19.94 (0.15)	27.95 (1.97)	28.46 (0.53)	28.62 (0.27)	27.00 (1.01)	28.82 (0.59)	20.40 (0.44)	
Cr ₂ O ₃	0.02 (0.02)	0.02 (0.01)	0.02 (0.04)	0.01 (0.00)	0.01 (0.02)	0.02 (0.03)	0.01 (0.01)	0.00 (0.00)	0.00 (0.00)	0.04 (0.03)	0.03 (0.03)	0.00 (0.00)	0.06 (0.00)	0.00 (0.00)	0.06 (0.00)	0.00 (0.00)	0.02 (0.05)	0.01 (0.00)	0.02 (0.04)	0.03 (0.08)	0.05 (0.08)	0.03 (0.80)	0.03 (0.36)	0.02 (0.13)	0.02 (1.55)	0.03 (0.40)	0.02 (0.06)	
FeO*	19.12 (0.55)	19.76 (0.69)	19.29 (0.26)	19.44 (0.33)	19.41 (0.24)	19.35 (0.55)	20.26 (0.86)	12.09 (0.20)	12.91 (0.52)	12.89 (0.39)	12.25 (0.36)	12.73 (0.36)	13.73 (0.36)	13.76 (0.36)	0.66 (0.09)	0.70 (0.09)	0.09 (0.05)	0.12 (0.00)	0.15 (0.04)	0.10 (0.08)	0.21 (0.08)	5.96 (0.80)	5.53 (0.36)	5.35 (0.13)	6.08 (1.55)	5.48 (0.40)	25.75 (0.06)	
MgO	6.95 (0.64)	6.41 (0.32)	6.41 (0.53)	10.83 (0.37)	6.91 (0.26)	6.94 (0.28)	6.53 (0.32)	0.02 (0.01)	0.00 (0.00)	0.01 (0.01)	0.01 (0.01)	0.00 (0.00)	0.01 (0.00)	0.02 (0.01)	0.00 (0.00)	0.01 (0.00)	0.00 (0.00)	0.01 (0.02)	0.01 (0.00)	0.00 (0.00)	0.01 (0.01)	2.44 (0.44)	2.27 (0.27)	2.08 (0.10)	2.52 (0.20)	2.10 (0.20)	15.30 (0.35)	
MnO	0.15 (0.03)	0.15 (0.07)	0.14 (0.08)	0.18 (0.04)	0.13 (0.05)	0.13 (0.05)	0.15 (0.04)	0.11 (0.04)	0.22 (0.14)	0.25 (0.03)	0.36 (0.42)	0.50 (0.03)	0.19 (0.03)	0.19 (0.03)	0.10 (0.03)	0.08 (0.03)	0.00 (0.03)	0.01 (0.03)	0.05 (0.04)	0.02 (0.02)	0.02 (0.01)	0.01 (0.01)	0.00 (0.03)	0.00 (0.01)	0.03 (0.01)	0.01 (0.05)	0.02 (0.02)	0.28 (0.04)
CaO	0.54 (0.01)	0.68 (0.38)	0.42 (0.32)	9.02 (0.96)	0.58 (0.29)	0.58 (0.20)	0.74 (0.22)	23.04 (0.14)	23.59 (0.42)	23.12 (0.03)	22.84 (0.42)	22.64 (0.03)	23.24 (0.03)	23.25 (0.03)	28.52 (0.03)	28.20 (0.03)	0.06 (0.03)	0.06 (0.03)	0.08 (0.04)	0.07 (0.02)	0.04 (0.01)	0.03 (0.01)	0.02 (0.03)	0.01 (0.01)	0.01 (0.05)	0.06 (0.02)	0.02 (0.04)	
Na ₂ O	7.19 (0.14)	7.23 (0.16)	7.35 (0.13)	2.58 (0.65)	7.17 (0.15)	7.12 (0.12)	7.11 (0.09)	0.00 (0.00)	0.05 (0.02)	0.01 (0.00)	0.01 (0.01)	0.01 (0.00)	0.03 (0.00)	0.01 (0.00)	0.03 (0.00)	0.01 (0.00)	11.97 (0.04)	12.13 (0.33)	11.60 (0.54)	12.19 (0.16)	12.30 (0.10)	0.33 (0.22)	0.40 (0.09)	0.46 (0.04)	0.26 (0.11)	0.41 (0.08)	0.00 (0.00)	
K ₂ O	0.01 (0.01)	0.02 (0.01)	0.02 (0.00)	0.31 (0.07)	0.02 (0.01)	0.01 (0.01)	0.03 (0.02)	0.01 (0.01)	0.01 (0.01)	0.01 (0.00)	0.00 (0.00)	0.00 (0.00)	0.00 (0.00)	0.00 (0.00)	0.01 (0.01)	0.00 (0.00)	0.02 (0.01)	0.02 (0.00)	0.03 (0.02)	0.02 (0.01)	0.04 (0.01)	9.88 (0.37)	9.64 (0.11)	9.61 (0.04)	9.86 (0.28)	9.72 (0.21)	0.00 (0.00)	
Total	98.21 (0.62)	98.19 (0.33)	98.18 (0.38)	97.68 (0.35)	97.66 (0.43)	98.19 (0.56)	97.86 (0.36)	97.87 (0.06)	96.09 (1.51)	98.01 (0.78)	97.97 (0.12)	97.57 (0.12)	98.11 (0.12)	98.68 (0.12)	98.60 (0.12)	98.33 (0.12)	100.91 (0.80)	101.30 (0.08)	102.31 (1.14)	101.63 (0.34)	101.97 (0.53)	98.58 (0.55)	98.03 (0.65)	97.56 (0.43)	97.51 (0.62)	97.67 (0.52)	87.97 (0.74)	
Si	7.93 (0.02)	7.87 (0.11)	7.98 (0.04)	7.47 (0.05)	7.91 (0.11)	7.92 (0.05)	7.88 (0.08)	2.99 (0.00)	2.99 (0.05)	2.97 (0.01)	2.98 (0.02)	2.99 (0.01)	3.02 (0.01)	3.00 (0.02)	1.01 (0.01)	1.01 (0.01)	2.8 (0.01)	2.97 (0.02)	3.00 (0.05)	2.97 (0.02)	2.96 (0.01)	3.37 (0.04)	3.36 (0.02)	3.36 (0.02)	3.40 (0.03)	3.34 (0.02)	2.75 (0.04)	
Ti	0.01 (0.00)	0.01 (0.01)	0.01 (0.00)	0.01 (0.01)	0.02 (0.01)	0.01 (0.01)	0.02 (0.01)	0.01 (0.00)	0.01 (0.01)	0.01 (0.00)	0.02 (0.02)	0.01 (0.00)	0.01 (0.00)	0.00 (0.00)	0.87 (0.00)	0.88 (0.00)	0.00 (0.00)	0.00 (0.00)	0.00 (0.00)	0.00 (0.00)	0.00 (0.00)	0.01 (0.00)	0.01 (0.00)	0.01 (0.00)	0.01 (0.00)	0.01 (0.00)	0.00 (0.00)	
Al	1.37 (0.05)	1.44 (0.08)	1.37 (0.08)	0.80 (0.11)	1.34 (0.12)	1.36 (0.09)	1.34 (0.07)	2.26 (0.03)	2.07 (0.04)	2.19 (0.04)	2.24 (0.03)	2.21 (0.03)	2.09 (0.04)	2.13 (0.03)	0.10 (0.01)	0.10 (0.01)	1.01 (0.01)	1.01 (0.00)	1.02 (0.01)	1.01 (0.01)	1.00 (0.00)	2.15 (0.13)	2.19 (0.04)	2.22 (0.02)	2.10 (0.04)	2.23 (0.04)	2.54 (0.07)	
Cr	0.00 (0.00)	0.00 (0.00)	0.00 (0.00)	0.00 (0.00)	0.00 (0.00)	0.00 (0.00)	0.00 (0.00)	0.00 (0.00)	0.00 (0.00)	0.00 (0.00)	0.00 (0.00)	0.00 (0.00)	0.00 (0.00)	0.00 (0.00)	0.00 (0.00)	0.00 (0.00)	0.00 (0.00)	0.00 (0.00)	0.00 (0.00)	0.00 (0.00)	0.00 (0.00)	0.00 (0.00)	0.00 (0.00)	0.00 (0.00)	0.00 (0.00)	0.00 (0.00)	0.00 (0.00)	
Fe*	2.27 (0.06)	2.35 (0.10)	2.29 (0.04)	2.40 (0.04)	2.32 (0.04)	2.30 (0.07)	2.43 (0.12)	0.79 (0.01)	0.87 (0.02)	0.85 (0.03)	0.81 (0.03)	0.84 (0.03)	0.90 (0.03)	0.90 (0.03)	0.02 (0.00)	0.02 (0.00)	0.00 (0.00)	0.00 (0.00)	0.01 (0.00)	0.00 (0.00)	0.01 (0.00)	0.33 (0.05)	0.30 (0.02)	0.29 (0.01)	0.34 (0.09)	0.30 (0.02)	2.27 (0.02)	
Mg	1.47 (0.14)	1.36 (0.06)	1.35 (0.12)	2.38 (0.09)	1.47 (0.06)	1.47 (0.07)	1.40 (0.07)	0.00 (0.00)	0.00 (0.00)	0.00 (0.00)	0.00 (0.00)	0.00 (0.00)	0.00 (0.00)	0.00 (0.00)	0.00 (0.00)	0.00 (0.00)	0.00 (0.00)	0.00 (0.00)	0.00 (0.00)	0.00 (0.00)	0.00 (0.00)	0.24 (0.05)	0.22 (0.03)	0.20 (0.01)	0.25 (0.02)	0.21 (0.02)	2.40 (0.03)	
Mn	0.02 (0.00)	0.02 (0.01)	0.02 (0.01)	0.02 (0.01)	0.02 (0.01)	0.02 (0.01)	0.02 (0.00)	0.01 (0.00)	0.02 (0.01)	0.02 (0.00)	0.02 (0.03)	0.03 (0.03)	0.01 (0.00)	0.01 (0.00)	0.00 (0.00)	0.00 (0.00)	0.00 (0.00)	0.00 (0.00)	0.00 (0.00)	0.00 (0.00)	0.00 (0.00)	0.00 (0.00)	0.00 (0.00)	0.00 (0.00)	0.00 (0.00)	0.00 (0.00)	0.00 (0.00)	
Ca	0.08 (0.00)	0.10 (0.06)	0.06 (0.05)	1.43 (0.16)	0.09 (0.04)	0.09 (0.03)	0.11 (0.04)	1.94 (0.01)	2.03 (0.00)	1.95 (0.02)	1.92 (0.03)	1.92 (0.03)	1.96 (0.03)	1.95 (0.03)	1.00 (0.00)	0.99 (0.00)	0.00 (0.00)	0.00 (0.00)	0.00 (0.00)	0.00 (0.00)	0.00 (0.00)	0.00 (0.00)	0.00 (0.00)	0.00 (0.00)	0.00 (0.00)	0.00 (0.00)	0.00 (0.00)	
Na	1.98 (0.03)	2.00 (0.03)	2.02 (0.03)	2.02 (0.18)	1.99 (0.03)	1.96 (0.03)	1.98 (0.02)	0.00 (0.00)	0.01 (0.00)	0.00 (0.00)	0.00 (0.00)	0.00 (0.00)	0.00 (0.00)	0.00 (0.00)	0.00 (0.00)	0.00 (0.00)	1.00 (0.01)	1.01 (0.02)	0.96 (0.05)	1.01 (0.01)	1.02 (0.01)	0.04 (0.03)	0.05 (0.01)	0.06 (0.00)	0.03 (0.01)	0.05 (0.01)	0.00 (0.00)	
K	0.00 (0.00)	0.00 (0.00)	0.00 (0.00)	0.06 (0.01)	0.00 (0.00)	0.00 (0.00)	0.01 (0.00)	0.00 (0.00)	0.00 (0.00)	0.00 (0.00)	0.00 (0.00)	0.00 (0.00)	0.00 (0.00)	0.00 (0.00)	0.00 (0.00)	0.00 (0.00)	0.00 (0.00)	0.00 (0.00)	0.00 (0.00)	0.00 (0.00)	0.00 (0.00)	0.82 (0.04)	0.80 (0.01)	0.80 (0.00)	0.83 (0.03)	0.82 (0.02)	0.00 (0.00)	
Total	15.13 (0.02)	15.16 (0.17)	15.11 (0.07)	15.29 (0.03)	15.16 (0.04)	15.14 (0.06)	15.18 (0.08)	8.00 (0.00)	8.00 (0.00)	8.00 (0.00)	8.00 (0.00)	8.00 (0.00)	8.00 (0.00)	8.00 (0.00)	3.00 (0.00)	3.00 (0.00)	5.00 (0.00)	5.00 (0.00)	5.00 (0.00)	5.00 (0.00)	5.00 (0.00)	6.97 (0.03)	6.95 (0.01)	6.95 (0.01)	6.97 (0.05)	6.96 (0.02)	10.86 (0.01)	

Table 4. Average composition of major elements (ox. wt %) and of recalculated structural formulae of minerals composing mafic rocks from the Ophiolitic Complex (numbers in brackets are standard deviations)

Sample Mineral Microstructural position No. analyses	Amphibole						Titanite		Plagioclase		Phengite	
	AK33A			AK36			AK33B	AK36	AK33A	AK36	AK33A	AK36
	Amp ₂ fine 3	Amp ₂ Core 3	Amp ₂ Rim 2	Amp ₂ fine 3	Amp ₂ Core 3	Amp ₂ Rim 6	Ttn ₂ 3	Ttn ₂ 5	Ab Porph 5	Ab Porph 12	Wm ₂ 5	Wm ₂ 3
SiO ₂	55.20 (0.24)	55.07 (0.20)	55.47 (0.18)	55.60 (0.35)	55.74 (0.32)	55.74 (0.46)	30.78 (0.31)	30.73 (0.24)	68.82 (0.28)	68.87 (0.30)	53.56 (0.60)	53.68 (0.87)
TiO ₂	0.07 (0.01)	0.04 (0.04)	0.03 (0.03)	0.14 (0.16)	0.06 (0.01)	0.03 (0.04)	36.39 (1.38)	36.68 (1.24)	0.01 (0.02)	0.01 (0.01)	0.08 (0.05)	0.11 (0.02)
Al ₂ O ₃	2.36 (0.79)	2.29 (0.08)	2.31 (0.30)	2.38 (0.66)	2.59 (0.42)	2.10 (0.46)	1.74 (0.63)	1.44 (0.60)	19.56 (0.14)	19.64 (0.20)	24.93 (0.85)	24.57 (0.88)
Cr ₂ O ₃	0.06 (0.04)	0.06 (0.05)	0.05 (0.03)	0.03 (0.04)	0.07 (0.04)	0.05 (0.04)	0.01 (0.01)	0.04 (0.05)	0.00 (0.00)	0.01 (0.01)	0.11 (0.06)	0.15 (0.03)
FeO*	19.10 (0.43)	20.73 (1.17)	20.64 (0.55)	19.20 (0.12)	19.75 (0.43)	19.21 (1.56)	1.09 (0.34)	1.13 (0.14)	0.11 (0.05)	0.06 (0.04)	5.14 (0.70)	4.78 (1.33)
MgO	10.92 (0.66)	9.79 (0.87)	9.73 (0.03)	10.43 (0.59)	10.01 (0.27)	10.67 (0.74)	0.04 (0.03)	0.04 (0.02)	0.01 (0.01)	0.01 (0.01)	3.50 (0.07)	3.73 (0.07)
MnO	0.15 (0.00)	0.15 (0.03)	0.12 (0.01)	0.15 (0.02)	0.12 (0.01)	0.15 (0.04)	0.02 (0.02)	0.01 (0.01)	0.01 (0.02)	0.02 (0.02)	0.01 (0.02)	0.00 (0.00)
CaO	3.47 (1.58)	2.26 (0.68)	1.64 (0.18)	2.01 (0.78)	1.12 (0.20)	2.31 (1.83)	28.06 (0.21)	28.07 (0.28)	0.01 (0.01)	0.01 (0.01)	0.04 (0.03)	0.01 (0.01)
Na ₂ O	5.36 (0.77)	6.23 (0.33)	6.42 (0.02)	6.44 (0.54)	6.68 (0.05)	6.06 (0.95)	0.02 (0.02)	0.05 (0.06)	11.54 (0.10)	11.57 (0.09)	0.11 (0.04)	0.11 (0.05)
K ₂ O	0.08 (0.05)	0.05 (0.02)	0.04 (0.01)	0.03 (0.00)	0.02 (0.01)	0.03 (0.01)	0.09 (0.06)	0.07 (0.10)	0.03 (0.01)	0.00 (0.01)	9.79 (0.53)	9.79 (0.17)
Total	96.78 (0.20)	96.67 (0.53)	96.43 (0.32)	96.42 (0.20)	96.18 (0.38)	96.35 (0.32)	98.25 (0.28)	98.25 (0.42)	100.10 (0.46)	100.19 (0.47)	97.26 (0.58)	96.93 (0.51)
Si	7.89 (0.02)	7.91 (0.05)	7.97 (0.01)	7.96 (0.06)	7.99 (0.03)	7.98 (0.04)	1.01 (0.01)	1.01 (0.01)	3.01 (0.01)	3.01 (0.01)	3.52 (0.02)	3.53 (0.02)
Ti	0.01 (0.00)	0.00 (0.00)	0.00 (0.00)	0.01 (0.02)	0.01 (0.00)	0.00 (0.00)	0.90 (0.03)	0.91 (0.03)	0.00 (0.00)	0.00 (0.00)	0.00 (0.00)	0.01 (0.00)
Al	0.40 (0.13)	0.39 (0.01)	0.39 (0.05)	0.40 (0.11)	0.44 (0.07)	0.35 (0.08)	0.07 (0.02)	0.06 (0.02)	1.01 (0.00)	1.01 (0.01)	1.93 (0.05)	1.91 (0.05)
Cr	0.01 (0.00)	0.01 (0.01)	0.01 (0.00)	0.00 (0.00)	0.01 (0.00)	0.01 (0.00)	0.00 (0.00)	0.00 (0.00)	0.00 (0.00)	0.00 (0.00)	0.01 (0.00)	0.01 (0.00)
Fe*	2.28 (0.05)	2.49 (0.15)	2.48 (0.06)	2.30 (0.02)	2.37 (0.06)	2.30 (0.19)	0.03 (0.01)	0.03 (0.00)	0.00 (0.00)	0.00 (0.00)	0.28 (0.04)	0.26 (0.08)
Mg	2.33 (0.14)	2.10 (0.17)	2.08 (0.00)	2.23 (0.13)	2.14 (0.05)	2.28 (0.15)	0.00 (0.00)	0.00 (0.00)	0.00 (0.00)	0.00 (0.00)	0.34 (0.01)	0.37 (0.01)
Mn	0.02 (0.00)	0.02 (0.00)	0.02 (0.00)	0.02 (0.00)	0.01 (0.00)	0.02 (0.00)	0.00 (0.00)	0.00 (0.00)	0.00 (0.00)	0.00 (0.00)	0.00 (0.00)	0.00 (0.00)
Ca	0.53 (0.24)	0.35 (0.10)	0.25 (0.03)	0.31 (0.12)	0.17 (0.03)	0.35 (0.28)	0.99 (0.01)	0.99 (0.01)	0.00 (0.00)	0.00 (0.00)	0.00 (0.00)	0.00 (0.00)
Na	1.49 (0.21)	1.74 (0.10)	1.79 (0.01)	1.79 (0.15)	1.86 (0.01)	1.68 (0.27)	0.00 (0.00)	0.00 (0.00)	0.98 (0.01)	0.98 (0.01)	0.01 (0.01)	0.01 (0.01)
K	0.01 (0.01)	0.01 (0.00)	0.01 (0.00)	0.01 (0.00)	0.00 (0.00)	0.01 (0.00)	0.00 (0.00)	0.00 (0.00)	0.00 (0.00)	0.00 (0.00)	0.82 (0.05)	0.82 (0.01)
Total	14.96 (0.02)	15.01 (0.03)	14.99 (0.01)	15.03 (0.03)	15.00 (0.01)	14.99 (0.06)	3.00 (0.00)	3.00 (0.00)	5.00 (0.00)	5.00 (0.00)	6.92 (0.05)	6.92 (0.03)

respect to white micas of mafic rocks from the CGC and MC. As already discussed by Zanchi *et al.* (2015), this comparison suggests that phengitic micas of meta-pillow basalts likely re-equilibrated with riebeckite under blueschist-facies conditions during a prograde, relatively HP, metamorphism.

5.b.4. Thermodynamic modelling

A P – T isochemical section was calculated with PERPLE_X software (Connolly, 2005), considering the bulk composition of sample AK14b and H_2O -saturated conditions, using the thermodynamic database and equation of state for H_2O of Holland & Powell (1998, upgraded 2002). No phase has been excluded from the calculation. Solution models of Holland & Powell (1998, 2003) were used for olivine, orthopyroxene, clinopyroxene, garnet, phengite, feldspar, epidote, chlorite and biotite. Two different solution models have been used to model Ca-amphibole and Na-amphibole from Dale *et al.* (2005), which require Fe_2O_3 and FeO concentrations. Fe^{3+} -rich minerals such as epidote also occurs in both HP–LT and syn- S_2 metamorphic event, and the use of a solid solution model for epidote is crucial to model their possible stability fields. For this reason, we measured the FeO and Fe_2O_3 concentration of the whole rock by chemical titration and considered FeO and Fe_2O_3 as distinct chemical components in the thermodynamic forward modelling. The phase diagram section reported in Figure 7 shows that the (pre- S_2) Cpx-free mineral association Na-Amp₁ + Wm₁ + Ttn₁ + Ep₁ + Pl₁ is stable in a narrow P – T range between 0.8 and 0.95 GPa and 410–460 °C, respectively. The appearance of chlorite in the S_2 Cpx-free and Bio-free mineral assemblage (blue text in Fig. 7) Amp₂ (core) + Chl + Wm₂ + Ep₂ (core) + Pl₂ occurs at similar temperature conditions and lower pressures, down to 0.65 GPa.

Comparing the Morghab metamorphic peak conditions with those of the Chah Gorbah and Ophiolite units (0.75–0.85 GPa and 350–400 °C) reported by Zanchi *et al.* (2015), the MC mafic schists experienced HP metamorphism before the development of the S_2 foliation as will be discussed later. It is worth noting that the thermodynamic modelling results are strongly supported by the microstructural evidence (Fig. 5).

Thermodynamic modelling of the stability of solid solutions with Fe^{3+} -bearing end-member minerals (i.e. epidote and Na-amphibole) requires the assumption that the bulk Fe^{2+}/Fe^{3+} ratio was constant during the entire metamorphic cycle of the rock. We therefore compared the P – T isochemical section of Figure 7 with a T – fO_2 isochemical section calculated at 0.9 GPa, which is portrayed in Figure 8. The starting composition is the same as that used in Figure 7, but considering FeO as total iron. The peak (pre- S_2) Na-Amp₁ + Wm₁ + Ttn₁ + Ep₁ + Pl₁ mineral association is stable at 460 °C and $\log fO_2 \cong -25.5$, corresponding to FMQ-1 (FMQ is the reference fayalite–magnetite–quartz buffer). It is worth noting that the stability of

epidote is strongly influenced by the oxidation state of the bulk composition, therefore by the Fe^{2+}/Fe^{3+} ratio of the rock. The fO_2 value calculated from forward modelling enables a back calculation of the expected FeO and Fe_2O_3 content of the whole rock using the equation of Kress & Carmichael (1988). The measured Fe^{2+}/Fe^{3+} ratio at $T = 450$ °C and $P = 1$ atm would be stable at $\log fO_2 = -24$, which is perfectly consistent with the values calculated in Figure 8, if we consider that fO_2 slightly decreases with increasing pressure. We can therefore assume that the Fe^{2+}/Fe^{3+} content used to reconstruct the P – T stability field of epidote- and Na-amphibole-bearing assemblage is representative of the composition of the rock at the pressure-peak conditions.

6. Discussion

The three main units constituting the gross part of the AMC show a complex structural pattern that is the result of at least three deformation events. The MC, CGC and OC were refolded together during the last deformation stage (D_3) and overthrust by the Lakh Marble unit (Zanchi *et al.* 2015). D_3 structure developments occurred at non- or very low-grade metamorphic conditions (Fig. 3e). The metamorphic evolution of the three units should then be related to pre- D_3 deformation stages.

Field structural analyses (Zanchi *et al.* 2015) individuated a regional foliation (S_2) that is almost parallel in the MC and CGC units, suggesting that it is probably related to the same deformation event that affected the two units during or after their tectonic coupling. However, the detailed study of microstructures and mineral chemistry of blueschist-facies mineral assemblages in the AMC rocks presented in this study suggests that the three units experienced tectonometamorphic evolutions that differed in some stages.

The spatial relationships between compositionally distinct amphiboles in the MC, CGC and OC mafic rocks point to a pre- S_2 (regional foliation) pressure peak in the MC. Amphiboles (Amp₁) included in plagioclase (Pl₁) and epidote (Ep₂) porphyroblasts are glaucophane or ferroglaucophane (Table 2; Fig. 6), whereas Amp₂, aligned along the main foliation (S_2), are calcic amphiboles (Amp₂ in Table 2). Deformation–recrystallization relationships thus indicate that peak pressure (0.80–0.95 GPa at T of 410–450 °C, Fig. 7) was reached by the MC mafic schists before the development of the S_2 foliation. Calcic amphiboles (Amp₂) and epidotes (Ep₂) syn-kinematic with the S_2 foliation display in turn a core–rim compositional zoning indicative of a pressure increase during or after the D_2 deformation event. Based on these data we can define a clockwise P – T path for the AMC (Fig. 9), with a blueschist-facies stage followed by greenschist re-equilibration at lower pressure and later underplating to greater depths. The amphibole chemical composition suggests that the late- S_2 metamorphic

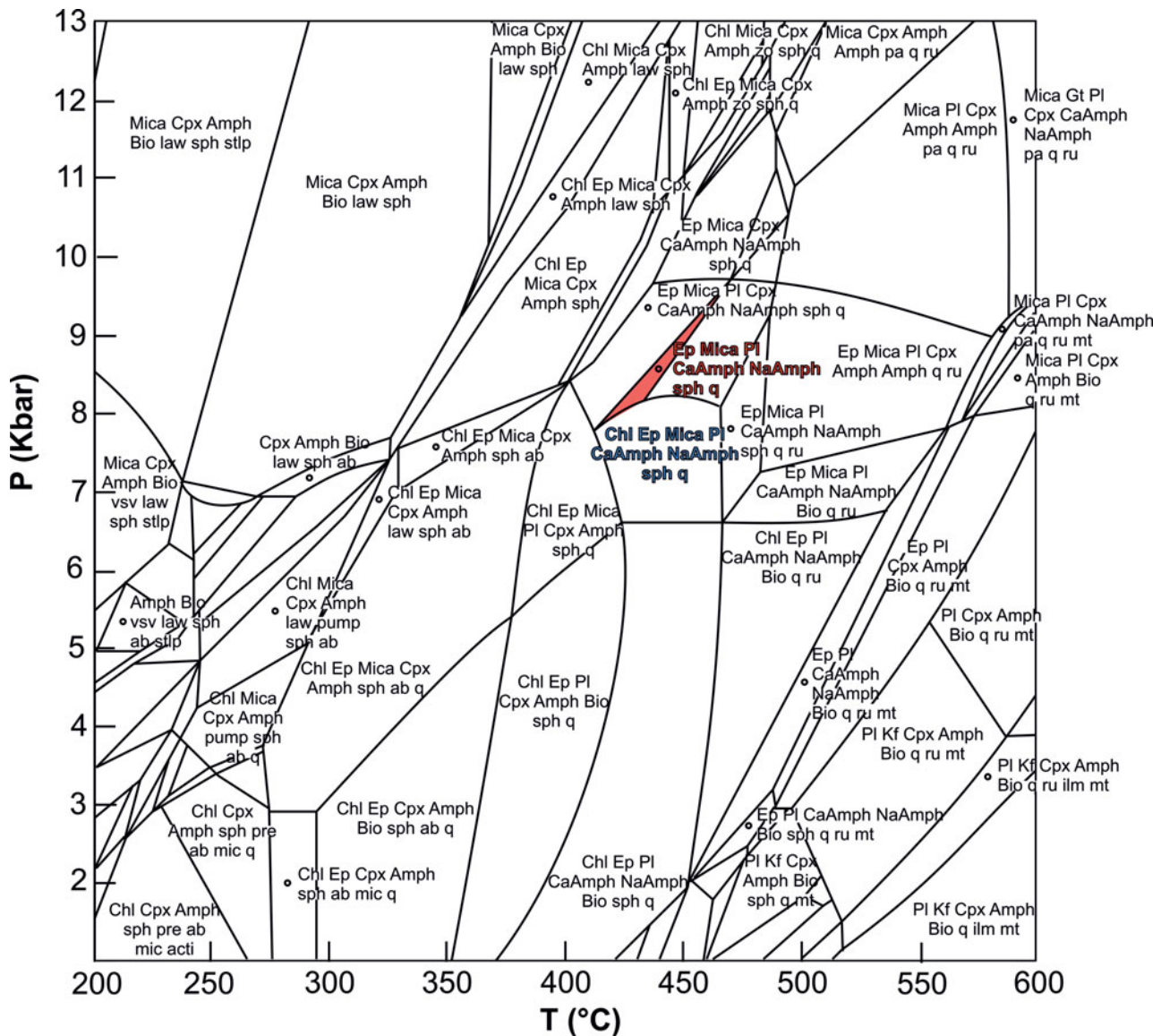


Figure 7. (Colour online) Isochemical P - T section for Morghab meta-basalt calculated in the system SiO_2 (50.27) – Al_2O_3 (14.42) – MgO (5.61) – CaO (7.27) – Na_2O (4.53) – K_2O (0.82) – TiO_2 (1.41) – FeO (8.57) – Fe_2O_3 (3.43). Values in brackets are oxide wt. %. The red area shows the hypothetical stability field of the relict HP paragenesis preserved in porphyroblastic epidote, as evidenced by microstructural and mineral chemistry analyses. Abbreviations for solid solution models: Amph – Ca-amphiboles and Na-amphiboles; Bio – biotite; Chl – chlorite; Ep – epidote; Cpx – clinopyroxene; Gt – garnet; Kfs – alkali feldspar; Mica – phengite; Pl – ternary feldspar. Abbreviations for phases: ab – albite; acti – actinolite; fctd – Fe-chloritoid; ilm – ilmenite; law – lawsonite; mic – microcline; mt – magnetite; q – quartz; pa – paragonite; pre – prehnite; pump – pumpellyite; ru – rutile; sph – titanite (sphene); stlp – stilpnomelane; vsv – vesuvianite; zo – zoisite. The paragenesis at pressure peak observed in thin-section is highlighted in red. The same equilibrium phase assemblage with chlorite in addition (blue text in figure) occurs at the same T , but a lower pressure with respect to the chlorite-free one.

stage did not reach the pressure-peak experienced by the MC mafic rocks during the pre- D_2 evolution.

The CGC and OC mafic rocks display a contrasting metamorphic evolution. HP–LT metamorphism is demonstrated to have followed a greenschist-facies metamorphic event as shown by microstructures and mineral chemistry. Sodic amphibole (Amp_2) in CGC rocks is aligned along the main foliation (S_2 , Fig. 5), whereas low- P actinolitic amphibole (Amp_1) is preserved as inclusions within Pl_1 and Ep_1 porphyroblasts which are pre-kinematic with respect to S_2 . The compositional variation of epidote, with syn- S_2 Ep_2 enriched in Fe^{3+} with respect to Ep_1 , and the growth of

rutile instead of titanite as the main Ti-bearing phase, could be considered as clues that point to a P increase during the D_2 deformation event. Nevertheless, special care should be taken as at low to medium pressure, the compositional variation of epidote also depends on $f\text{O}_2$, coexisting Ca–Al silicates and H_2O -content (e.g. Grapes & Hoskin, 2004).

The meta-pillow basalts provide less information on the deformation–metamorphism relationships as they are substantially non-deformed. A poorly developed primary foliation (S_1) is defined by the SPO of greenschist-facies minerals, with actinolitic amphibole (Amp_1) and chlorite as the main mineral phases. The

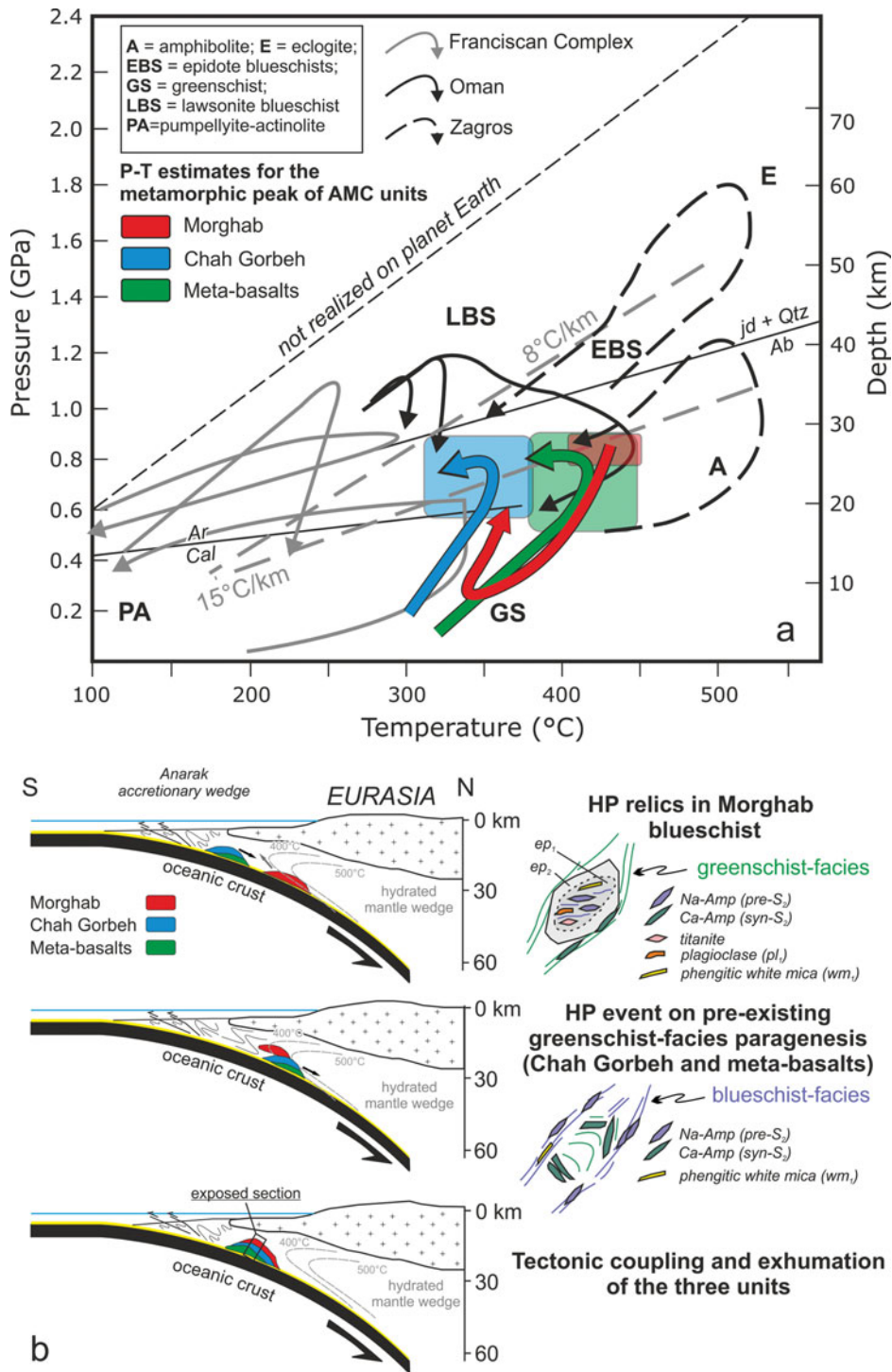


Figure 9. (Colour online) (a) P - T estimates and inferred P - T paths of the CGC, MC and OC blueschists. P - T estimates for the GCG and OC metabasites are from Zanchi *et al.* (2015). Representative reconstructed P - T paths for blueschists from the Franciscan subduction complex (Ernst, 1988; Banno *et al.* 2000; Ukar & Cloos, 2014), Oman (Yamato *et al.* 2007; Agard *et al.* 2010) and Zagros (Angiboust *et al.* 2016) are reported for comparison. Metamorphic facies are from Evans (1990). (b) Cartoon depicting the suggested geodynamic scenario in which the tectonic units of the AMC acquired their contrasting P - T evolutionary paths.

of HP-phase assemblages. This stage could be related to an early heating during subduction initiation, before the depression of the geotherms by continuous subduction of the oceanic crust. An alternative hypothesis is that this low-pressure stage is related to seafloor metamorphism overprinted during subduction. Ocean floor metamorphism is commonly associated with diffuse veining and intense metasomatism, which are both ab-

sent in the AMC units. Quartz- and calcite-bearing veins occur in the pillow meta-basalts (Fig. 4d), but they cross-cut both pillows and sheared domains with a blueschist-facies overprint (Fig. 4b). This suggests that veining represents a late-stage feature, post-dating the burial and exhumation of the OC unit. The same holds true also for the mafic schist and associated rocks of the CGC (Zanchi *et al.* 2015).

The counter-clockwise P – T paths experienced by CGC and OC were likely due to early heating when they were underthrust beneath the southern Eurasia margin at the beginning of subduction (Fig. 9).

Such counter-clockwise P – T paths are common within evolved accretionary wedges, when mafic rocks derived from the subducting oceanic crust or sediments scraped off the evolving prism are accreted in the early stages of subduction and later buried to increasing depth while geotherms are progressively depressed (Cloos, 1982).

On the other hand, the P – T path of the MC is rather peculiar: an early HP–LT metamorphic stage is followed by greenschist-facies re-equilibration with a further pressure increase as suggested by amphibole and epidote compositional zoning. P – T estimates made by forward thermodynamic modelling (fig. 24 in Zanchi *et al.* 2015) indicate similar pressures of the CGC and OC relative to the pre- S_2 metamorphic peak, but at higher T (Fig. 9). Dynamic metamorphism represented by the syn- S_2 metamorphic stage re-equilibrated the HP–LT phase assemblages at greenschist-facies conditions. The chemical compositions (Fig. 6) of amphibole and epidote that grew during this greenschist-facies event point to a late- to post-deformation pressure increase. Summarizing, (Table 2) the MC mafic rocks experienced a clockwise P – T path, with an early HP–LT stage followed by exhumation at lower depths (greenschist-facies re-equilibration) and subsequent pressure increase likely due to re-subduction within the accretionary wedge.

Despite the possible difference in P – T paths experienced by the three units, a temperature/depth gradient of *c.* 15 °C km⁻¹ seems to be the best estimate for the peak pressure in all units (Fig. 9).

Counter-clockwise P – T paths within exhumed accretionary prisms are well known for block-in-matrix subduction mélanges, like the Franciscan Complex (Ukar, 2012; Ukar & Cloos, 2014), but are less common in HP–LT complexes made of coherent tectonic units. The Hajiabad blueschists of the Zagros orogen (Agard *et al.* 2006; Angiboust *et al.* 2016) display instead such features (Fig. 9). Despite different metamorphic peak conditions, several units underwent an initial heating stage during underplating, followed by HP–LT dynamic metamorphism. Geochronological data suggest that tectonic units reached pressure peak at different times (Angiboust *et al.* 2016). The occurrence and preservation of counter-clockwise P – T paths are likely favoured for tectonic units that were underplated in the first subduction stages, along a relatively hot (15–17 °C km⁻¹) geothermal gradient. Geotherms are then progressively depressed as the subduction zone evolves and early subducted units can be exhumed along a cold (< 10 °C km⁻¹) subduction channel.

The age of HP–LT metamorphism in the AMC units is debated. Bagheri & Stampfli (2008) proposed an Early Permian age (285 Ma) for blueschists of the CGC, and a ‘Variscan’ age for the HP–LT metamorph-

ism of the MC, suggesting that the two units formed in distinct times and palaeotectonic settings. However, these geochronological data are highly debatable (Zanchi *et al.* 2015) as microstructural and chemical features of the dated minerals are loosely constrained. To our knowledge metamorphism and deformation of AMC units should be constrained to pre-Sakmarian (*c.* 300 Ma or older) times (Zanchi *et al.* 2015) and no robust data exist on the age of HP–LT metamorphism. Even if we take as valid the available geochronological data of the HP–LT metamorphism of the AMC, we need to consider that in the context of a long-lasting subduction (e.g. several tens of millions of years) the subducted rocks could reach the metamorphic peak at different ambient conditions and at different times (e.g. Gerya, Stockhert & Perchuk, 2002; Ukar, 2012). Therefore, the meta-basalts and the blueschists of the CGC and MC, even if they recorded contrasting P – T evolutions and were possibly metamorphosed at different ages, could still be considered as parts of a single accretionary complex.

The nature and provenance of the continental blocks that collided with the southern Eurasian margin is also controversial. The Anarak block strongly differs from the Upper Palaeozoic successions of Central and North Iran that record an extensional evolution related to the opening of the Neo-Tethys that caused the northward drift of Iran (Angiolini *et al.* 2007; Gaetani *et al.* 2009). A possible provenance, discussed in Zanchi *et al.* (2015), is that the AMC was part of the accretionary wedge developed above the Palaeo-Tethys subduction zone. In NE Iran, the Variscan–Cimmerian complexes of Binalood and Fariman (Sheikholeslami & Kouhpeyma, 2012; Zanchetta *et al.* 2013) recorded the upper plate history of the Palaeo-Tethys subduction. The AMC could be originally placed to the SW of the Fariman complex and later shifted westwards to its present-day position in the framework of the large counter-clockwise rotation along a vertical axis that affected Central Iran from Triassic time (Muttoni *et al.* 2009; Mattei *et al.* 2015).

7. Conclusions

The AMC of Central Iran is made of several units among which three of them, the Morghab, Chah Gorbah and meta-basalts complexes, have been metamorphosed at HP–LT conditions within the blueschist facies.

At least three deformation events have been recognized in the MC and CGC. The second deformation stage is responsible for the development of the regional foliation (S_2) that is generally concordant in the two units. Microstructural investigations and microprobe analyses demonstrated that the main foliation developed at blueschist-facies and greenschist-facies conditions for the CGC and MC units, respectively. The main fabric element of the CGC and MC thus formed when the two units were at different depths within the accretionary wedge.

The reconstruction of the deformation–metamorphism relationships and P – T estimates of the metamorphic stages allowed the definition of a clockwise P – T path for the MC and a counter-clockwise path for CGC and meta-basalts of the OC. P – T conditions at metamorphic peak were of 410–450 °C at 0.78–0.9 GPa for the MC, 390–440 °C at 0.6–0.9 GPa for the meta-basalts and 320–380 °C at 0.6–0.9 GPa for the CGC.

The presented data suggest that the three units reached almost the same depth (*c.* 25 km) within the Anarak accretionary wedge, but followed different subduction–exhumation paths that resulted in a contrasting P – T evolution.

Acknowledgements. This paper results from the PRIN 2010/2011 Project BIRTH AND DEATH OF OCEANIC BASINS: GEODYNAMIC PROCESSES FROM RIFTING TO CONTINENTAL COLLISION IN MEDITERRANEAN AND CIRCUM-MEDITERRANEAN OROGENS and the DARIUS PROGRAMME. We are grateful to Vachik Hairapetian (Department of Geology, Esfahan Branch, Islamic Azad University, Iran) for providing us information on the age of the Lakh Marble. Comments and suggestions by Yann Rolland and an anonymous reviewer helped us to improve the quality of the paper. G. Capponi is warmly thanked for the editorial handling of the paper. We are grateful to the Geological Survey of Iran (Teheran branch) for its continuous support during several years of common research activities in Central Iran.

References

- AGARD, P., MONIÉ, P., GERBER, W., OMRANI, J., MOLINARO, M., MEYER, B. & YAMATO, P. 2006. Transient, synobduction exhumation of Zagros blueschists inferred from P – T , deformation, time, and kinematic constraints: implications for Neotethyan wedge dynamics. *Journal of Geophysical Research: Solid Earth* **111** B11401, doi: [10.1029/2005JB004103](https://doi.org/10.1029/2005JB004103).
- AGARD, P., SEARLE, M. P., ALSOP, G. I. & DUBACQ, B. 2010. Crustal stacking and expulsion tectonics during continental subduction: P – T deformation constraints from Oman. *Tectonics* **29**, TC5018, doi: [10.1029/2010TC002669](https://doi.org/10.1029/2010TC002669).
- ANGIBOUST, S., AGARD, P., GLODNY, J., OMRANI, J. & ONCKEN, O. 2016. Zagros blueschists – episodic underplating and long-lived cooling of a subduction zone. *Earth and Planetary Science Letters* **443**, 48–58.
- ANGIOLINI, L., GAETANI, M., MUTTONI, G., STEPHENSON, M. H. & ZANCHI, A. 2007. Tethyan oceanic currents and climate gradients 300 my ago. *Geology* **35**, 1071–4.
- BAGHERI, S. & STAMPFLI, G. M. 2008. The Anarak, Jandaq and Posht-e-Badam metamorphic complexes in central Iran: new geological data, relationships and tectonic implications. *Tectonophysics* **451**, 123–55.
- BALINI, M., NICORA, A., BERRA, F., GARZANTI, F., LEVERA, M., MATTEI, M., MUTTONI, M., ZANCHI, A., BOLLATI, I., LARGHI, C., ZANCHETTA, S., SALAMATI, R. & MOSSAVVARI, F. 2009. The Triassic stratigraphic succession of Nakhlak (central Iran), a record from an active margin. In *South Caspian to Central Iran Basins* (eds M. F. Brunet, M. Wilmsen & J. W. Granath), pp. 287–321. Geological Society of London, Special Publication no. 312.
- BANNO, S., SHIBAKUSA, H., ENAMI, M., WANG, C.-L. & ERNST, W. G. 2000. Chemical fine structure of Franciscan jadeitic pyroxene from Ward Creek, Cazadero area, California. *The American Mineralogist* **85**, 1795–8.
- BERRA, F., ZANCHI, A., ANGIOLINI, L., VACHARD, D., VEZZOLI, G., ZANCHETTA, S., BERGOMI, M., JAVADI, H. R., KOUHPEYMA, M. 2017. The upper Palaeozoic Godar-e-Siah Complex of Jandaq: evidence and significance of a North Palaeotethyan succession in Central Iran. *Journal of Asian Earth Sciences* **138**, 272–90.
- BUCHS, D. M., BAGHERI, S., MARTIN, K., HERMANN, J. & ARCULUS, R. 2013. Paleozoic to Triassic ocean opening and closure preserved in Central Iran: constraints from the geochemistry of meta-igneous rocks of the Anarak area. *Lithos* **172–173**, 267–87.
- CLOOS, M. 1982. Flow mélange: numerical modelling and geologic constrain on their origin in the Franciscan subduction complex, California. *Geological Society of America Bulletin* **93**, 330–44.
- CLOOS, M. & SHREVE, R. L. 1988a. Subduction-channel model of prism accretion, mélange formation, sediment subduction, and subduction erosion at convergent plate margins: 1. background and description. *Pure and Applied Geophysics* **128**, 455–500.
- CLOOS, M. & SHREVE, R. L. 1988b. Subduction-channel model of prism accretion, mélange formation, sediment subduction, and subduction erosion at convergent plate margins: 2. implications and discussion. *Pure and Applied Geophysics* **128**, 501–45.
- CONNOLLY, J. A. D. 2005. Multivariable phase diagrams: an algorithm based on generalized thermodynamics. *American Journal of Science* **290**, 666–718.
- DALE, J., POWELL, R., WHITE, R. W., ELMER, F. L. & HOLLAND, T. J. B. 2005. A thermodynamic model for Ca-Na clin amphiboles in Na₂O-CaO-FeO-MgO-Al₂O₃-SiO₂-H₂O-O for petrological calculations. *Journal of Metamorphic Geology* **23**, 771–91.
- ERNST, W. G. 1973. Blueschist metamorphism and P – T regimes in active subduction zones. *Tectonophysics* **17**, 255–72.
- ERNST, W. G. 1988. Tectonic history of subduction zones inferred from retrograde blueschist P – T paths. *Geology* **16**, 1081–4.
- EVANS, B. W. 1990. Phase relations of epidote-blueschists. *Lithos* **35**, 3–23.
- GAETANI, M., ANGIOLINI, L., UENO, K., NICORA, A., STEPHENSON, M. H., SCIUNNACH, D., RETTORI, R., PRICE, G. D. & SABOURI, J. 2009. Pennsylvanian–Early Triassic stratigraphy in the Alborz Mountains (Iran). In *South Caspian to Central Iran Basins* (eds M. F. Brunet, M. Wilmsen & J. W. Granath), pp. 79–128. Geological Society of London, Special Publication no. 312.
- GERYA, T. & STOCKHERT, B. 2006. Two-dimensional numerical modeling of tectonic and metamorphic histories at active continental margins. *International Journal of Earth Sciences* **95**, 250–74.
- GERYA, T. V., STOCKHERT, B. & PERCHUK, A. L. 2002. Exhumation of high-pressure metamorphic rocks in a subduction channel: a numerical simulation. *Tectonics* **21**, 6–1–6–19.
- GHAsemi, A. M. & TALBOT, C. J. 2006. A new tectonic scenario for the Sanandaj-Sirjan Zone (Iran). *Journal of Asian Earth Sciences* **26**, 683–93.
- GRAPES, R. H. & HOSKIN, P. W. 2004. Epidote group minerals in low-medium pressure metamorphic terranes. In *Epidotes* (eds A. Liebscher & G. Franz), pp. 301–55. Reviews in Mineralogy and Geochemistry 56.

- HOLLAND, T. J. B. & POWELL, R. 1998. An internally consistent thermodynamic data set for phases of petrologic interest. *Journal of Metamorphic Geology* **16**, 309–43.
- HOLLAND, T. J. B. & POWELL, R. 2003. Activity-composition relations for phases in petrological calculations: an asymmetric multicomponent formulation. *Contributions to Mineralogy and Petrology* **145**, 492–501.
- HSU, K. J. 1968. Principles of mélanges and their bearing on the Franciscan-Knoxville paradox. *Geological Society of America Bulletin* **79**, 1063–74.
- KRESS, V. C. & CARMICHAEL, I. S. E. 1988. Stoichiometry of the iron oxidation reaction in silicate melts. *American Mineralogist* **73**, 1267–74.
- KRUSE, P. D. & ZHURALEV, A. YU. 2008. Middle–Late Cambrian Rankenella–Girvanella reefs of the Mila Formation Northern Iran. *Canadian Journal of Earth Sciences* **45**, 619–39.
- MATTEI, M., CIFELLI, F., MUTTONI, G. & RASHID, H. 2015. Post-Cimmerian (Jurassic–Cenozoic) paleogeography and vertical axis rotation of Central Iran and the Alborz Mountains. *Journal of Asian Earth Sciences* **102**, 92–101.
- MEL'NIKOV, B. N., ROZANOV, A. YU., SUSOV, M. V. & FONIN V., D. 1986. Pervye arkhoeotsiaty iz nizhengo kembriya tsentral'nogo Irana (First archaeocyaths from the Lower Cambrian of central Iran). *Izvestiya, Akademiya Nauk SSSR* **7**, 134–8.
- MUTTONI, M., MATTEI, M., BALINI, M., ZANCHI, A., GAETANI, M. & BERRA, F. 2009. The drift history of Iran from the Ordovician to the Triassic. In *South Caspian to Central Iran Basins* (eds M. F. Brunet, M. Wilmsen & J. W. Granath), pp. 7–29. Geological Society of London, Special Publication no. 312.
- ŞENGÖR, A. M. C. 1979. Mid-Mesozoic closure of Tethys and its implications. *Nature* **279**, 590–3.
- SHARKOVSKI, M., SUSOV, M. & KRIVYAKIN, B. 1984. *Geology of the Anarak Area (Central Iran)*. Explanatory Text of the Anarak Quadrangle Map 1:250000. Geological Survey of Iran, V/O “Tecnoexport” USSR Ministry of Geology Reports, 19.
- SHEIKHOESLAMI, M. R. & KOUHPEYMA, M. 2012. Structural analysis and tectonic evolution of the eastern Binalud Mountains, NE Iran. *Journal of Geodynamics* **61**, 23–46.
- TORABI, G. 2012. Late Permian post-ophiolitic trondhjemites from Central Iran: a mark of subduction role in growth of Paleozoic continental crust. *Island Arcs* **21**, 215–29.
- UKAR, E. 2012. Tectonic significance of low-temperature blueschists blocks in the Franciscan mélange at San Simeon, California. *Tectonophysics* **568–569**, 154–69.
- UKAR, E. & CLOOS, M. 2014. Low-temperature blueschist-facies mafic blocks in the Franciscan mélange, San Simeon, California. *Geological Society America Bulletin*, B30876.1, doi: [10.1130/B30876.1](https://doi.org/10.1130/B30876.1).
- WILSON, A. D. 1955. Determination of ferrous iron in rocks and minerals. *Bulletin of the Geological Survey of Great Britain* **9**, 56–8.
- YAMATO, P., AGARD, P., GOFFÉ, B., DE ANDRADE, V., VIDAL, O. & JOLIVET, L. 2007. New, high precision P–T estimates for Oman blueschists: implications for obduction, nappe stacking and exhumation processes. *Journal of Metamorphic Geology* **25**, 657–82.
- YOKOYAMA, T. & NAKAMURA, E. 2002. Precise determination of ferrous iron in silicate rocks. *Geochemica and Cosmochemica Acta* **66**, 1085–93.
- ZANCHETTA, S., BERRA, F., ZANCHI, A., BERGOMI, M., CARIDROIT, M., NICORA, M. & HEIDARZADEH, G. 2013. The record of the Late Palaeozoic active margin of the Palaeotethys in NE Iran: constraints on the Cimmerian orogeny. *Gondwana Research* **24**, 1237–66.
- ZANCHI, A., MALASPINA, N., ZANCHETTA, S., BERRA, F., BENCIOLINI, L., BERGOMI, M., CAVALLO, A., JAVADI, H. R. & KOUHPEYMA, M. 2015. The Cimmerian accretionary wedge of Anarak, Central Iran. *Journal of Asian Earth Sciences* **102**, 45–72.
- ZANCHI, A., ZANCHETTA, S., GARZANTI, E., BALINI, M., BERRA, F., MATTEI, M. & MUTTONI, G. 2009. The Cimmerian evolution of the Nakhlak-Anarak area, central Iran, and its bearing for the reconstruction of the history of the Eurasian margin. In *South Caspian to Central Iran Basins* (M. F. Brunet, M. Wilmsen & J. W. Granath, eds), pp. 261–86. Geological Society of London, Special Publications no. 312.